

# The Role of Mesoscale Convective Systems in Precipitation in the Tibetan Plateau region

Julia Kukulies<sup>1</sup>, Deliang Chen<sup>1</sup>, Julia Curio<sup>1</sup>

<sup>1</sup>Regional Climate Group, Department of Earth Sciences, University of Gothenburg, Gothenburg, Sweden

## Key Points:

- Mesoscale convective systems were tracked in the Tibetan Plateau region for the past two decades
- Co-locations of brightness temperatures with precipitation indicate reduced numbers of mesoscale convective systems over the Tibetan Plateau
- Precipitation and large-scale environments associated with mesoscale convective systems were compared between different subregions

---

Corresponding author: Deliang Chen, [deliang@gvc.gu.se](mailto:deliang@gvc.gu.se)

This article has been accepted for publication and undergone full peer review but has not been through the copyediting, typesetting, pagination and proofreading process, which may lead to differences between this version and the [Version of Record](#). Please cite this article as [doi: 10.1029/2021JD035279](https://doi.org/10.1029/2021JD035279).

This article is protected by copyright. All rights reserved.

## Abstract

Mesoscale convective systems (MCSs) have been identified as an important source of precipitation in the Tibetan Plateau (TP) region. However, the characteristics and structure of MCS-induced precipitation are not well understood in this location. Infrared (IR) satellite imagery has been used for MCS tracking, but cirrus clouds or cold surfaces can lead to false MCS classification over mountain regions. Here, we combine brightness temperatures from IR imagery with satellite precipitation estimates from GPM IMERG and track MCSs over the TP, at the boundary of the TP (TPB), and in the surrounding lower-elevation plains (LE), between 2000 and 2019. In most parts of LE and TPB, MCSs produced 50 to 80 % of the total summer precipitation (60 to 90% of summer heavy precipitation), whereas MCSs over the TP account for below 10 % of the total summer precipitation (10 to 30 % of summer heavy precipitation). Our results also show that MCSs that produce the largest amounts of heavy precipitation are characterised by longevity and large extents rather than by high intensities. These are mainly located in the populous areas south and east of the TP. A tracking of meso- $\beta$  convective systems over the TP shows that small-scale convection makes a large contribution to total and heavy precipitation. This suggests that more localised convective systems are important for the regional water cycle over the higher terrain and highlights the importance of convective-scale modelling to improve our understanding of precipitation dynamics in the TP region.

## Plain Language Summary

Storm systems that extend over several hundred kilometres can represent a risk to people's lives and livelihoods, as they may lead to flooding, extreme winds and heavy rainfall. The Tibetan Plateau (TP) has received increasing attention over the last few decades because it has experienced drastic changes in the water cycle as a response to global warming. Although it is known that large storm systems develop in the populous surrounding regions of the TP, the rainfall characteristics from these storms are not well understood. It is difficult to identify storm systems in satellite images over high mountain regions, because high clouds and low surface temperatures can give signals similar to those of storm clouds. We therefore used a new method to track large storm systems in satellite images over the TP to clarify their role in the water cycle. Our results show that most of the storms that produce heavy rainfall occurred in the regions south and east of the TP. Storm systems over the TP are generally smaller in size and shorter in duration, which means that climate model simulations at high spatial resolution are needed to further investigate them.

## 1 Introduction

Mesoscale convective systems (MCSs) are organised convective storm complexes, which extend over several hundreds of kilometres and produce large areas of convective and stratiform precipitation (Houze, 2004). MCSs have more complex dynamics than unicellular convective storms, but are primarily defined by their spatial extent (Houze Jr, 2004). Many different forces can drive mesoscale organisation of convection. Thus, the structure and precipitation characteristics of MCSs can take different forms depending on the region of genesis and underlying processes. In the continental mid-latitudes, MCSs often occur in areas downstream regions of high-altitude regions, as MCS formation is related to mountain flow dynamics. On the leeside of the Rocky Mountains (over the Great Plains) (Hitchcock et al., 2019; Cheeks et al., 2020; Hu et al., 2020), in the West-African Sahel (Redelsperger et al., 2002; Vondou et al., 2010; Klein et al., 2018) and in the European Alps (Morel & Senesi, 2002; Feidas, 2017), MCSs produce a significant portion of the total precipitation in a season and can lead to severe weather.

61 The Tibetan Plateau (TP) covers an area of two and a half million square kilome-  
62 tres and is the world's most extensive mountain region. The headwaters of most of Asia's  
63 major rivers are located in the mountains of the TP, and their discharge regimes are mainly  
64 controlled by monsoonal precipitation (Zhang et al., 2013). A distinct characteristic of  
65 the TP is its high elevation and steep topography, which results in complex interactions  
66 between local mountain features and large-scale atmospheric dynamics. Many studies  
67 have identified MCSs as one of the most important precipitation-producing mechanisms  
68 over the TP (Tao & Ding 1981; Wang et al., 1987; Li et al., 2008; Sugimoto & Ueno, 2010;  
69 Hu et al., 2017). Some extreme rainfall and flood hazards in the heavily populated down-  
70 stream regions to the south and east of the TP have been attributed to MCSs, as have  
71 mesoscale vortices that form over the TP (Yasunari & Miwa, 2006; Shi et al., 2008; Xi-  
72 ang et al., 2013; Rasmussen & Houze, 2012). This demonstrates that MCSs can pose a  
73 direct threat to life, people's livelihoods, crop yields and infrastructure. On the other  
74 hand, MCSs play an important role in the hydrological cycle, as they may account for  
75 a significant amount of the annual or seasonal rainfall, for example in North America (Fritsch  
76 et al., 1986; Feng et al. 2021). Convection-permitting model simulations project increases  
77 in MCS intensity for some regions (Prein et al., 2017; Fitzpatrick et al., 2020) and con-  
78 vective precipitation is likely to increase at much larger rates than a precipitation increase  
79 of 7 % per degree of warming, which would correspond to the Clausius-Clapeyron rela-  
80 tion (Berg et al., 2013; Ban et al., 2015). It is therefore crucial that we understand the  
81 scales and formation processes of heavy precipitation, particularly for mountain regions  
82 like the TP, which are likely to experience drastic environmental changes due to global  
83 warming (Bibi et al., 2018; Yao et al., 2019).

84 Although many studies on convection in the TP region focus on MCSs, the main  
85 drivers behind the systems and their significance for current and future precipitation regimes  
86 are not well understood. It is not clear how characteristics of MCSs that are generated  
87 over the TP differ from those of monsoon-related convective systems that occur along  
88 the Himalayas (Houze et al., 2007; Romatschke et al., 2010). A number of studies that  
89 investigated MCSs at elevations higher than 3,000 m above sea level (a.s.l.) have iden-  
90 tified the central and eastern parts of the TP as the main source regions for convection  
91 (Jiang et al. 2002; Li et al. 2008; Sugimoto & Ueno, 2010; Hu et al., 2017). However,  
92 due to the difficulty in attributing precipitation events to specific storm systems, the im-  
93 portance of MCSs for precipitation could only be roughly estimated. Radar observations  
94 of clouds over the southern Himalayas show clear signatures of convection (Houze et al.,  
95 2007) with high radar reflectivities over a height range between 5 and 14 km a.s.l. dur-  
96 ing summer (Kukulies et al., 2019). This may indicate organised convection in this re-  
97 gion, but the poor temporal resolution and spatial coverage of spaceborne radar obser-  
98 vations raise the question of whether this feature really can be attributed to MCSs or  
99 if it derives from isolated deep convection. Additionally, convective cells can be misclas-  
100 sified when infrared (IR) satellite imagery is used to track MCSs in a high mountain re-  
101 gion and image scenes include cold cirrus cloud tops (Rossow & Schiffer, 1999; Yuan &  
102 Houze, 2010) or cold surfaces under clear-sky conditions that result in a similar IR bright-  
103 ness temperature (Esmaili et al., 2016). Observation-based studies of MCSs are there-  
104 fore more limited than model studies for the TP region and often cover only a few years,  
105 because high-resolution satellite records of more than a decade in length have only re-  
106 cently become available. It is crucial that we establish an accurate climatology of MCSs  
107 and understand their importance for precipitation, in order to advance our knowledge  
108 about precipitation dynamics in the TP region and to evaluate how well MCSs charac-  
109 teristics are represented in regional climate model simulations. The effect of MCSs on  
110 precipitation is key to an improved understanding of the drivers and scales of heavy pre-  
111 cipitation which in turn is necessary for more accurate estimates of future changes of pre-  
112 cipitation regimes and extreme events.

113 This study aims to describe MCS characteristics in the TP region using a novel track-  
114 ing method to interpret satellite observations covering the past two decades (i.e. from

2000 to 2019). To provide a broad overview of different types of MCSs, we compare MCSs over the TP with MCSs that cross the TP boundary (TPB) and MCSs that develop over the surrounding lower-elevation (LE) regions. We focus on the structure and characteristics of MCS-induced precipitation, the contribution of MCSs to seasonal and heavy precipitation as well as the large-scale environments that are associated with different MCS types.

We have organised this paper into four further sections. In Section 2, we compare MCS tracking methods of previous studies and describe the tracking algorithm and datasets used in this study. We also briefly explain the implementation of different MCS standards, to test the sensitivity of the tracking to different thresholds and criteria. In Section 3, we present a comparison of the different tracking methods and an overview of the spatial and temporal characteristics of MCS tracks as well as their precipitation features and associated large-scale atmospheric conditions. Section 4 discusses the role of MCSs in precipitation, retrieval uncertainties and possible driving mechanisms for MCS formation. Finally, a summary and the main conclusions are given in Section 5.

## 2 Data and Methods

### 2.1 Previous MCS studies

One of the most commonly used methods to identify MCSs is to detect contiguous areas of brightness temperature minima in IR satellite imagery. A specific type of MCS is a so-called mesoscale convective complex (MCC), originally defined by Maddox (1980). MCCs are cloud systems with a contiguous area of at least 100 000 km<sup>2</sup>, within which the maximum temperature is -32°C (241 K) and which includes a region of at least 50,000 km<sup>2</sup>, within which the maximum temperature is -52°C (221 K). An additional criterion is that these two conditions must persist for at least six hours for an MCC to be identified. Many studies have used a similar approach for global and regional MCS tracking (e.g. Rossow et al., 1999; Zheng et al., 2008; Esmaili et al., 2016; Huang et al., 2018). However, there is a wide range of thresholds used for brightness temperatures and minimum areas, dependent on whether the aim is to capture the entire evolution of the cloud system or focus on the deep convective part.

Table 1 summarises the tracking criteria used in previous studies that focused on MCSs over the TP or in South-East Asia. Brightness temperature thresholds vary between 219 K and 245 K over minimum areas that range from 1,000 km<sup>2</sup> to 50,000 km<sup>2</sup>. The highly varying thresholds reflect that there is no common standard for what defines a MCS in this region. Hence, the large differences in the amount of tracked MCSs per year are not only explained by the different domain sizes and time periods, but also by the different criteria chosen to define a MCS (Table 1). Most studies that only focused on the high altitudes of the TP have used minimum extents of  $\leq 5,000$  km<sup>2</sup>. These smaller, and consequently more short-lived, systems correspond to the meso- $\beta$  scale (horizontal dimensions of 20 to 200 km) according to the definition of Orlanski (1975), whereas the tracking studies that focused on larger areas in South-East Asia were predominantly designed to identify MCSs at the meso- $\alpha$  scale (horizontal dimensions 200 to 2,000 km).

Some of the studies listed in Table 1 have used global databases for convection tracking (e.g. Li et al., 2008) or thresholds that are also used in global analyses for MCS identification (Guo et al., 2006). However, using universal thresholds can be problematic in a mountain environment like the TP, where low surface temperatures from high mountain tops can be confused with high cloud tops from deep convective clusters, particularly at night and during winter. This has, for example, been discussed in Esmaili et al. (2016), who presented a global cloud cluster tracking with unrealistically high amounts of convective cloud clusters over the TP during winter when only brightness temperatures are used. The atmospheric transmittance at wavelengths corresponding to the IR

165 channels used for tracking ( $\sim 10.8 \mu\text{m}$ ) is relatively high, while surface emissivity at these  
166 wavelengths is generally low for dry regions (Schädlich et al., 2001). This means that re-  
167 trieved clear-sky brightness temperatures are on average lower than the actual surface  
168 temperatures, which poses an additional risk of confusing cold surfaces with high cloud  
169 tops in dry high-altitude regions.

Accepted Article

**Table 1.** Comparison of different MCS tracking methods used for East Asia and the TP region

Region	Period	Threshold	Extra criterion	Min Extent	Min duration	Reference	Tracks/year (season)
80105°E, 2740°N	1998	241 K		1000 km <sup>2</sup>	3 h	Guo et al. (2006)	749 (Jun-Aug)
75105°E, 2540°N	1998-2001	245 K	221 K cold core	27,000 km <sup>2</sup>	-	Li et al. (2008)	160 (Jun-Aug)
80-145 °E, 10-55° N	1996-2006	221 K		50,000 km <sup>2</sup>	-	Zheng et al. (2008)	-
70103°E, 2940°N > 3500 m	1998-2006	219 K		4,000 km <sup>2</sup>	6 hrs	Sugimoto and Ueno (2010)	290
75105°E, 2540°N > 3,000 m	1998-2004	245 K	optical depth $\leq 23$	25,000 km <sup>2</sup>	3 hrs	Hu et al. (2016)	106 (Jun-Aug)
106113°E, 2835°N	2000-2016	221 K no 2005		5,000 km <sup>2</sup>	3 hrs	Yang et al. (2019)	20 (May-Aug)
80150°E, 055°N	2016	235 K	max area =160 000 km <sup>2</sup>	10,000 km <sup>2</sup>	3 hrs	Chen et al. (2019)	41,334 (Apr-Sep)
75103°E, 2640°N > 3,000 m	2000 - 2016 no 2005	221 K		5,000 km <sup>2</sup>	3 hrs	Mai et al. (2021) (May-Sep)	609
102.58121.58°E, 21.0838.08°N	2008 - 2016	3 mm h <sup>-1</sup>		3,600 km <sup>2</sup>	6 hrs	Li et al. (2020)	420 (Mar-Nov)
105-123°E, 28-35°N 105° - 123°E, 20-27°N	2014 - 2018	241 K	225 K cold core	60 000 km <sup>2</sup>	6 hrs	Cui et al. (2020)	30 (May-Sep)

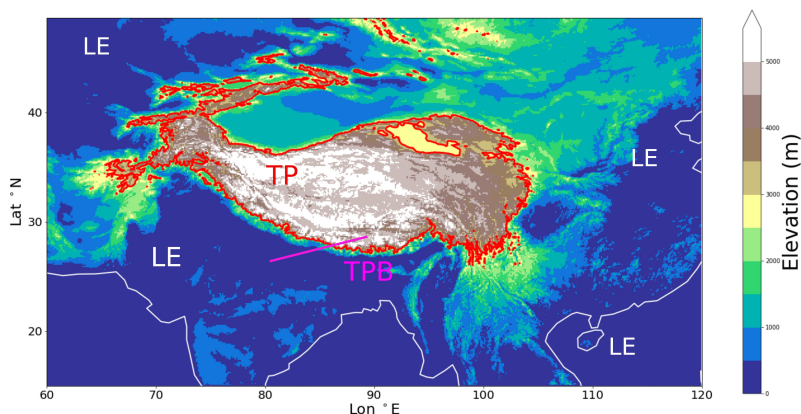


**Figure 1.** Study area ( $15 - 50^{\circ}\text{N}$ ,  $60 - 120^{\circ}\text{E}$ ) for regional MCS tracking. The colours show elevations [m a.s.l.] and the red line indicates the 3,000 m boundary of the TP. MCSs are divided into systems located outside of this boundary (LE), systems over the TP, and systems which cross the 3,000 m boundary during their lifetime (TPB).

170 Another risk of exclusively using IR brightness temperatures as a proxy for con-  
 171 vective activity in mountain regions is that convective systems can also be confused with  
 172 cirrus or stratiform cloud shields that are not necessarily the remnants of a storm sys-  
 173 tem. Kukulies et al. (2019) found that cirrus clouds are among the most frequent cloud  
 174 types over the central and southern parts of the TP between May and September. Thus,  
 175 it is likely that these cloud shields do not always originate from old convection. The high  
 176 number of MCS tracks that has been identified by Chen et al. (2019) (Table 1) reveals,  
 177 for instance, potential issues when the brightness temperature threshold is set too low  
 178 and when no additional data or criteria are used to assure that the low brightness tem-  
 179 peratures are linked to deep convection. To address the above-named issues, we followed  
 180 a similar approach to Feng et al. (2021) who created an updated global MCS dataset  
 181 based on an objective tracking method that combines IR imagery with precipitation data  
 182 and therefore reduces misclassifications of MCSs attributable to cirrus cloud layers and  
 183 cold surfaces.

## 184 2.2 Data and Tracking algorithm

185 Figure 1 shows the domain ( $15 - 50^{\circ}\text{N}$ ,  $60 - 120^{\circ}\text{E}$ ) in which the MCS tracking  
 186 was performed. The study area encompasses regions with substantially different precipi-  
 187 tation regimes, such as the Indo-Gangetic Plain, which is dominated by frequent mon-  
 188 soon depressions (Hurley & Boos, 2015; Boos et al., 2017) and the generally drier TP.  
 189 Considering such a wide area with diversified background climates, this study provides  
 190 a regional overview of MCSs, allowing those over the TP to be compared with those that  
 191 are initiated over more populous areas in the downstream regions. In this study, we there-  
 192 fore distinguish between three main types of systems: MCSs and precipitation events that  
 193 are initiated within the 3,000 m boundary of the plateau (TP), MCSs that cross the 3,000  
 194 m elevation boundary during their lifetime (TPB), and MCSs and precipitation events  
 195 at lower elevations (LE), outside the 3,000 m boundary (Fig. 1).

196 We used half-hourly satellite precipitation estimates from the Global Precipitation  
 197 Measurement Mission (GPM) in combination with brightness temperatures from IR im-

198 agery. The merged and angle-corrected brightness temperatures used in this study are  
199 provided by NCEP/CPC (National centres for Environmental Prediction/Climate Pre-  
200 diction centre) and were acquired by various sensors on board Meteosat, GMS/Himawari,  
201 Meteosat and GOES (Janowiak et al., 2017). The dataset can be downloaded from the  
202 data provider NASA GES DISC at 30 min resolution and with 4 km grid spacing. In or-  
203 der to obtain the same spatial resolution as the satellite precipitation data product GPM  
204 IMERG V06 (Huffman et al., 2019), which has a spatial resolution of  $0.1^\circ$ . To facilitate  
205 co-locating the two datasets, we regridded the brightness temperature data to match the  
206 GPM IMERG grid using first-order conservative mapping with the software Climate Data  
207 Operators (<https://code.mpimet.mpg.de/projects/cdo>). The tracking was performed  
208 in 30 min time steps to match the original temporal resolution of both datasets, for the  
209 period 2000 to 2019.

210 The tracking procedure consists of three main steps: 1) cloud feature detection using  
211 IR brightness temperatures, 2) linking of cloud features over time and 3) applying  
212 additional criteria based on co-locations with precipitation. Using the python package  
213 *tobac* (Heikenfeld et al., 2019), cloud features were identified in each time step in the re-  
214 gridded field of IR brightness temperatures ( $T_b$ ). The tracking library allows for smooth-  
215 ing the input field using a Gaussian filter. However, after testing different smoothing op-  
216 tions, we set the Gaussian filter to 0.5, which results in a minimal smoothing of the bright-  
217 ness temperatures and keeps the details of the cloud structure in the original data. To  
218 detect cloud features, we adapted the brightness temperature threshold of 221 K used  
219 in the original paper by Maddox (1980) and more recently in the same study region by  
220 Zheng et al. (2008). Because the focus of this paper is on MCSs with potentially large  
221 impacts on surface precipitation, we performed a tracking at the meso- $\alpha$  scale that re-  
222 quires a minimum cloud area of 50,000 km<sup>2</sup>. A cloud feature is hence defined as a con-  
223 tiguous area over 50,000 km<sup>2</sup> with brightness temperatures  $\leq 221$  K. In summer, cloud  
224 top temperatures below 221 K correspond to cloud top heights of about 10 km a.s.l. over  
225 the TP (Chen et al., 2018), which let us assume that brightness temperatures below this  
226 threshold are likely to be associated with deep convection at least during the warm sea-  
227 son.

228 Once cloud features have been identified in each time step, these features were linked  
229 over time based on their location and propagation speed. This was done by predicting  
230 the location of the cloud feature in the next time step using its average propagation speed  
231 from the previous time steps (or the average propagation speed of the closest feature for  
232 the first time step). Potential features within a restricted radius around the predicted  
233 location were then identified and the closest feature was connected with the trajectory,  
234 if its location was within a realistic distance to the previous cloud feature. More details  
235 about this linking method can be found in Heikenfeld et al. (2019). To be retained as  
236 a potential MCS, the minimum area of 50,000 km<sup>2</sup> has to persist for at least 3 hours (6  
237 time steps). Due to limited computational resources the feature linking was performed  
238 on yearly aggregated files, which means that MCSs at the boundary between two years  
239 appear as separate tracks. However, this does not significantly affect the results, since  
240 most MCSs in the study region occur during the summer season (see Section 3.2). It should  
241 also be noted that the merging and splitting of MCSs does not have any explicit treat-  
242 ment in the algorithm, but results in the survival of the MCS with the most similar travel  
243 direction (Heikenfeld et al., 2019). This way, we can identify long-lived MCSs that grow  
244 upscale when multiple cells merge into one larger MCS.

245 To assure that identified cloud features are indeed precipitation-producing systems  
246 with a region of deep convection, we filtered the connected cloud features based on two  
247 additional criteria that have been suggested by Yuan and Houze (2010) and Chen et al.  
248 (2018): the presence of a cold core reflected by an even higher temperature threshold within  
249 the cloud feature and the presence of heavy rainfall during the MCS lifetime. To be clas-  
250 sified as a MCS, brightness temperatures had to drop below 200 K (as in Yuan and Houze

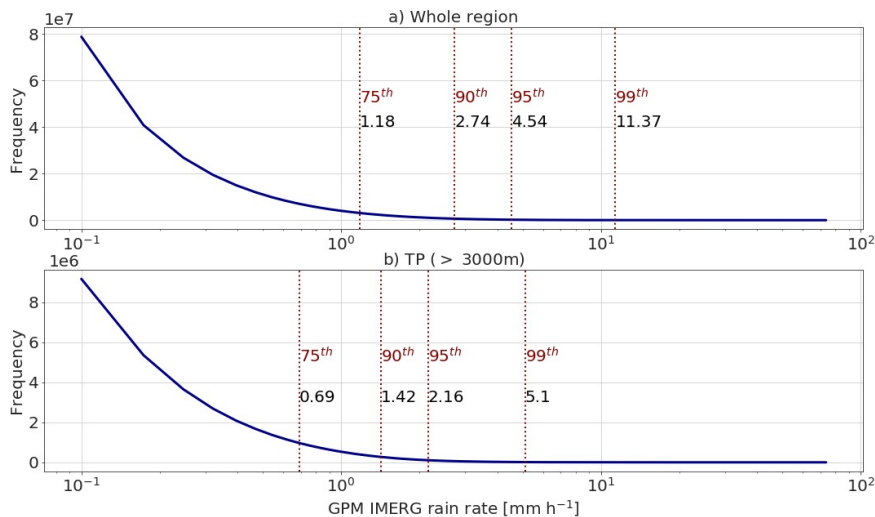


**Figure 2.** PDF and percentiles of hourly rain rates from GPM IMERG v06 2000 - 2019 for a) the whole study area (15 – 50 ° N, 60 – 120 ° E) and b) the TP > 3,000 m a.s.l.

(2010)) and contain an area that is at least 10 % of the minimum cloud area threshold of 50,000 km<sup>2</sup> (or 5,000 km<sup>2</sup> for meso- $\beta$ ) with rain rates above 5 mm h<sup>-1</sup> once during the MCS lifetime (as in Chen et al. (2018)). The precipitation threshold was chosen based on the evaluation of the probability density function (PDF) of IMERG precipitation pixels in the study region. The PDF shows that a rain rate of 5 mm h<sup>-1</sup> corresponds approximately to the 95<sup>th</sup> percentile of all hourly rain rates (Fig. 2).

In summary, a MCS in this paper is defined as a contiguous area of  $\leq 221$  K over at least 50,000 km<sup>2</sup> that persists for at least 3 hours, develops an area below 200 K and a precipitating area with rain rates  $\geq 5$  mm h<sup>-1</sup>). The tracking procedure and criteria are visualised in Figure 3. If the cloud feature in one time step does not fulfil the minimum area and brightness temperature criteria anymore, it is regarded as dissipated.

We also performed a meso- $\beta$  tracking over the TP that requires an area of at least 5 000 km<sup>2</sup> below the same threshold (221 K), as suggested in Mai et al. (2021). These systems are referred to as TCSs (Tibetan Convective Systems) and be used to discuss small-scale convective systems in the mountainous region. Systems that grow into meso- $\alpha$  systems at a later stage are excluded from this subgroup, so that the characteristics of systems that do not grow larger than meso- $\beta$  scale can be compared to the systems from the meso- $\alpha$  tracking. The meso- $\beta$  tracking is hence limited to systems that develop *at most* dimensions at the meso- $\beta$ -scale, whereas the meso- $\alpha$  tracking contains MCSs that grow upscale (which means that these may have been meso- $\beta$  systems before they reached meso- $\alpha$  dimensions). The purpose of tracking cloud features at two different spatial scales is to investigate the role of convective systems at the lower bounds of the mesoscale over the TP compared to larger MCSs. Due to limited computational resources, the meso- $\beta$  tracking could not be implemented for the entire study area as it would result in too many cloud feature combinations that had to be assessed to determine linkages across time steps. In the surrounding downstream regions, the focus is thus on convective systems at the meso- $\alpha$  scale, which we assume are more important for severe events and interactions with the large-scale atmospheric circulation.

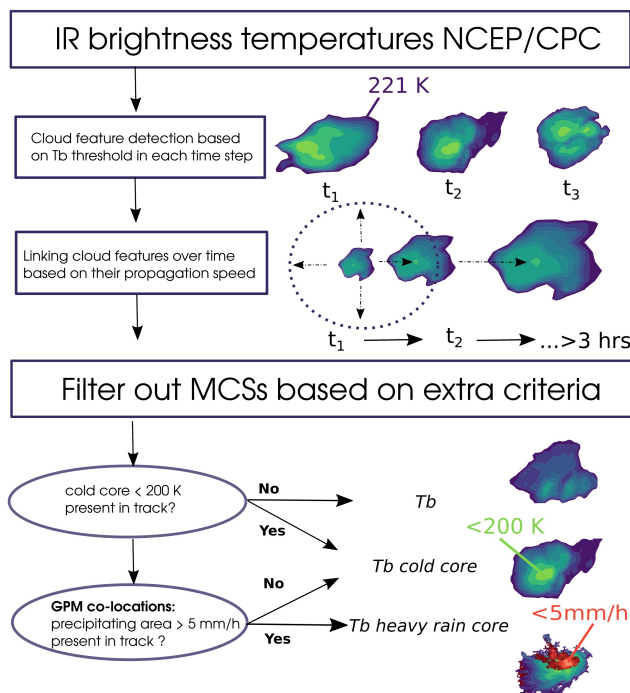


**Figure 3.** Flow chart and visualisation of MCS tracking procedure and criteria.

### 2.3 Analysis of MCS types and associated precipitation features

All tracked MCSs were assigned to one of four classes based on their dominant propagation direction (eastward or westward) and genesis location. These are denoted as TPB + TP east, TPB + TP west, LE east and LE west, where TPB + TP refers to MCSs over and at the boundary of the TP and LE refers to systems in the lower elevated surrounding regions that do not cross the 3,000 m boundary of the TP during any stage in their lifetime (Fig. 1). TP systems are defined as MCSs that have their cloud feature (221 K contour) within the 3,000 m boundary in the first detected time step, whereas TPB systems are defined as MCSs that show at least one time step where more than half of the cloud feature is located within the 3,000 m boundary. We focus on east-moving and west-moving systems because these were the two dominant propagation directions. East-moving MCSs reflect the transport of weather systems by mid-latitude westerlies and the other propagation directions result from an interaction between westerlies, the southerly Indian summer monsoon circulation and the easterly flow of the East Asian Monsoon. The propagation directions were determined using least-square fitting of all centre locations that belong to the same MCS track, so that MCSs that move along curved lines are assigned to the direction of their regression line.

The motivation for separating MCS trajectories into TPB + TP and LE was to distinguish between MCSs that originate at higher elevations and/or interact with the topography compared with MCSs in the plains. We used the cloud feature characteristics at each time step (area, brightness temperature intensity, precipitation features) and the characteristics of the track that describe the MCS evolution (lifetime, total precipitation, total heavy precipitation, propagation direction) to compare the different MCS types. Since the python package *tobac* allows for feature tracking using multiple thresholds, each identified cloud feature was also assigned to an intensity category (see Section 3.3.3). The intensity categories are defined as contiguous areas within the detected

cloud feature where a specific brightness temperature threshold is exceeded (between 190 K and 221 K).

To investigate the importance of MCS-associated precipitation for the water cycle, the total amount of precipitation was calculated for each of the detected cloud features and compared to the total seasonal precipitation received in each grid cell for the period 2000 to 2019. An MCS-associated precipitation feature is defined by all matched precipitation pixels within the detected cloud feature. We also included contiguous precipitation up to  $1.0 \text{ mm h}^{-1}$  outside of the cloud feature when it was directly connected to the main precipitation feature, in order to take account of stratiform precipitation behind or around the convective core. Because other precipitation-forming mechanisms than MCSs may dominate the total annual and seasonal precipitation in some subregions, we also examined the importance of MCS-associated rainfall for heavy precipitation events only. The range of rainfall intensities that are typically used to classify convective precipitation is wide (Gaal et al., 2014) and what can be called heavy or extreme precipitation depends on the regional conditions. After the evaluation of the PDF of hourly rain rates estimated by GPM IMERG (Fig. 2), we refer to heavy precipitation in the study region as precipitation produced by rain rates exceeding  $5 \text{ mm h}^{-1}$ . This rain rate threshold corresponds to the 99<sup>th</sup> percentile of rain rates over the TP and to the 95<sup>th</sup> in the surrounding monsoon-affected areas in the GPM IMERG dataset.

## 2.4 Sensitivity tests

It is important to note that the atmospheric variable selected as a proxy for storms and convection (e.g. brightness/cloud top temperature, outgoing longwave radiation, precipitation, vorticity or geopotential) determines the spatial and temporal characteristics of the tracked MCSs. There are many advantages to using precipitation, as it is a key component in the water cycle that has direct impacts on hydrology and society. It is also straightforward to compare precipitation tracks with model and reanalysis data, whereas IR brightness temperatures as seen by satellites are usually not available as a standard output variable from models. However, the part of a MCS in which precipitation is produced is usually smaller and more short-lived than the cloud system as a whole. Hence, using precipitation as a proxy for convection provides a more limited view of both the structure and evolution of tracked storm systems compared to brightness/ cloud top temperature.

To understand the implications of different MCS tracking methods on the key statistical features, we tested our tracking with four different methods. First, we performed tracking using only brightness temperatures ( $T_b$ ) with the temperature threshold of 221 K for the cloud feature identification. We then added the cold core criterion ( $T_b$  *cold core*) and the heavy rain criterion ( $T_b$  *heavy rain core*) that were described in Section 2.2. The MCS criteria for each tracking method are also summarised in Figure 3.

We also tested the sensitivity of the minimum area threshold for the heavy rain core, but no significant differences could be detected between 1 and 25 grid cells. Finally, we also implemented a tracking based on precipitation only, following the criteria used in Li et al. (2020) with minimum rain rates of  $3 \text{ mm h}^{-1}$  over a minimum area of  $3\,600 \text{ km}^2$  persisting for at least 6 hours (*Precip*). Considering the PDF of rain rates in the TP region compared to the surroundings (Fig. 2), this threshold represents a reasonable compromise to track precipitation cells in the more humid parts of the study domain as well as over the drier TP.

Table 2 summarises the criteria of the four different methods for the meso- $\alpha$  and meso- $\beta$  tracking as well as the number of MCSs identified in each tracking. The tested criteria are the same for the meso- $\beta$  tracking over the TP, to check whether the effect of the criteria also depends on region and scale. The number of MCS tracks in Table 2 is substantially higher when only precipitation cells are tracked (*Precip*) than for the other

**Table 2.** Criteria and total number of tracks for different tracking methods from 2000 to 2019

Test	Threshold	Extra criterion	Min extent [km <sup>2</sup> ]	Min time [hrs]	MCS tracks [avg per year]
meso- $\alpha$ tracking					
$T_b$	$\leq 221$ K		50,000	$\geq 3$	1,787
$T_b$ cold core	$\leq 221$ K	200 K	50,000	$\geq 3$	1,305
$T_b$ heavy rain core	$\leq 221$ K	10% $> 5$ mm h <sup>-1</sup>	50,000	$\geq 3$	1,267
<i>Precip</i>	$\geq 3$ mm h <sup>-1</sup>		3,600	$\geq 6$	4,680
meso- $\beta$ tracking					
$T_b$	$\leq 221$ K		5,000	$\geq 3$	1,283
$T_b$ cold core	$\leq 221$ K	200K	5,000	$\geq 3$	447
$T_b$ heavy rain core	$\leq 221$ K	10% 5 mm h <sup>-1</sup>	5,000	$\geq 3$	429

356 tracking methods. However, as will be shown in more detail in the next section, the area  
 357 distribution of the precipitation cells reveals much smaller spatial extents. Furthermore,  
 358 because tracked precipitation events are not always as continuous in time and space as  
 359 in the clearest cases of well-developed MCSs, the tracking results in many more individ-  
 360 ual cells. The additional criteria result in fewer MCS tracks compared to the  $T_b$  track-  
 361 ing, meaning that there are large cloud clusters  $> 221$  K that do not produce precipi-  
 362 tation (Table 2). This effect is particularly visible for the meso- $\beta$  tracking that has been  
 363 limited to the TP, presumably due to the previously mentioned concerns regarding cold  
 364 surfaces and cirrus clouds (see Section 2.1). Interestingly, the difference in the total num-  
 365 ber of tracks between  $T_b$  *cold core* and  $T_b$  *rain core* is very small for both the meso- $\alpha$   
 366 tracking and meso- $\beta$  tracking, meaning that the cold core criterion seems to automat-  
 367 ically assure that heavy rainfall is produced in most of the identified cloud features. In  
 368 the next Section, we present more detailed MCS characteristics for each tracking method.

### 369 3 Results

#### 370 3.1 Comparison of tracking methods

371 Figure 4a exemplifies co-located IR brightness temperatures with GPM IMERG  
 372 precipitation data for the study area. The snapshot shows a mature MCS on July 20<sup>th</sup>,  
 373 2008 and the succeeding plots show the evolution of the MCS track (Fig. 4b-e). The MCS  
 374 persisted for 18.5 hours and produced substantial amounts of heavy rainfall in the down-  
 375 stream region to the east of the TP. We used this well-known event, which was likely trig-  
 376 gered by a Tibetan Plateau vortex (Curio et al., 2019), as a case study to check whether  
 377 our tracking algorithm is able to capture the evolution of the system. In this example,  
 378 the amount of precipitation over time follows approximately the evolution of the cloud  
 379 area and peaks about six hours after the initiation, just before the cloud area reaches  
 380 its maximum (Fig. 4g).

381 For other MCS cases, however, the lifetime of contiguous heavy precipitation may  
 382 be much shorter than the lifetime of the cloud cluster it is embedded in. As the chosen  
 383 tracking criteria can have a substantial effect on the main characteristics of a MCS cli-  
 384 matology, we summarise the key features of tracked MCSs identified by the four differ-  
 385 ent tracking methods ( $T_b$ ,  $T_b$  *cold core*,  $T_b$  *heavy rain core*, *Precip*) in Figure 5. The high  
 386 number of *Precip* tracks in each month compared to the other tracking methods can partly  
 387 be explained by the smaller area threshold that needs to be met (Table 2), but also by  
 388 the fact that precipitation in a MCS may cease and be re-initiated into the same cloud  
 389 cluster (Fig. 5a). On top of that, precipitation is not necessarily contiguous in time and  
 390 space, but can occur as separate cells that are not identified as the same system in the  
 391 *Precip* tracking and hence result in larger numbers of individual tracks. The main dif-  
 392 ference between  $T_b$  compared to  $T_b$  *cold core* and  $T_b$  *heavy rain core* is the higher num-  
 393 ber of tracks for  $T_b$  that are identified between January and April. This can mainly be  
 394 attributed to features over the cold TP that are probably mistakenly identified as MCSs,  
 395 as shown in Figure 6.

396 The diurnal cycle for MCSs identified using *Precip* has multiple peaks (Fig. 5b),  
 397 whereas the other tracking methods are marked by a bimodal distribution with a clear  
 398 afternoon and a night/early morning peak. This difference in initiation time can also be  
 399 a side effect from the fact that *Precip* is limited to the MCS features that produce pre-  
 400 cipitation, while the other tracking methods capture the evolution of the MCSs more com-  
 401 pletely, including non-precipitating hours. In addition, the *Precip* tracking includes smaller  
 402 systems, since the area threshold has to be set relatively low, in order to capture most  
 403 systems that produce a contiguous area with heavy precipitation. Even though we cap-  
 404 tured *Precip* systems which have on average longer lifetimes than the majority of the cloud  
 405 cells (Fig. 5c), these have much smaller spatial extents that barely overlap with the MCS  
 406 area distributions derived from the other three tracking methods (Fig. 5d). The rela-

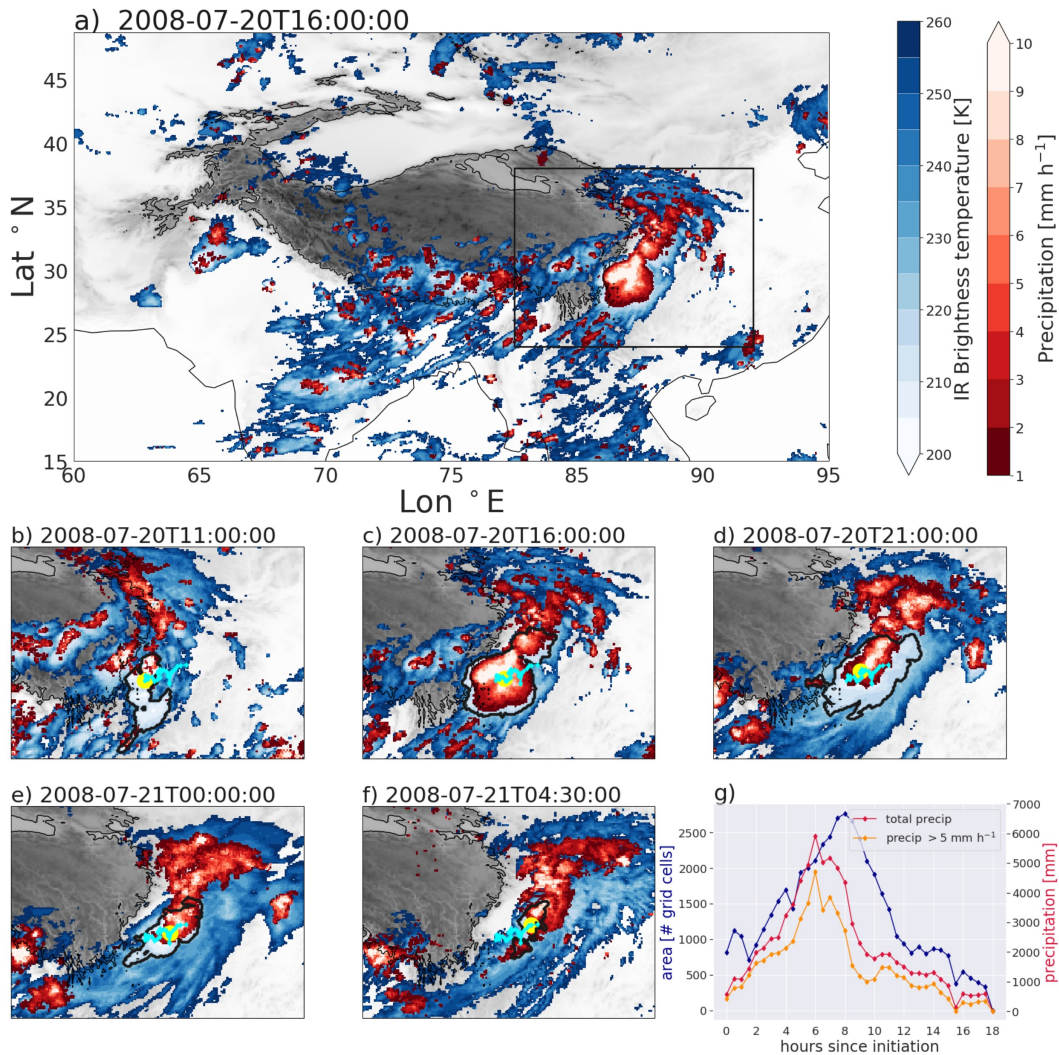


**Figure 4.** Example of a tracked MCS at the eastern boundary of the TP on 20-21<sup>th</sup> July, 2008. The upper panel shows a snapshot of half-hourly IR brightness temperatures and GPM IMERG precipitation (a). The evolution of the tracked cloud and precipitation feature are shown in the following panels (b-f), where the black line indicates the MCS centre locations at the preceding and succeeding time steps and the yellow dot marks the MCS centre location in the imaged time step. The evolution of the cloud feature area (blue), total precipitation (red) and total precipitation  $>5 \text{ mm h}^{-1}$  (orange) is shown in the time series graph (g).

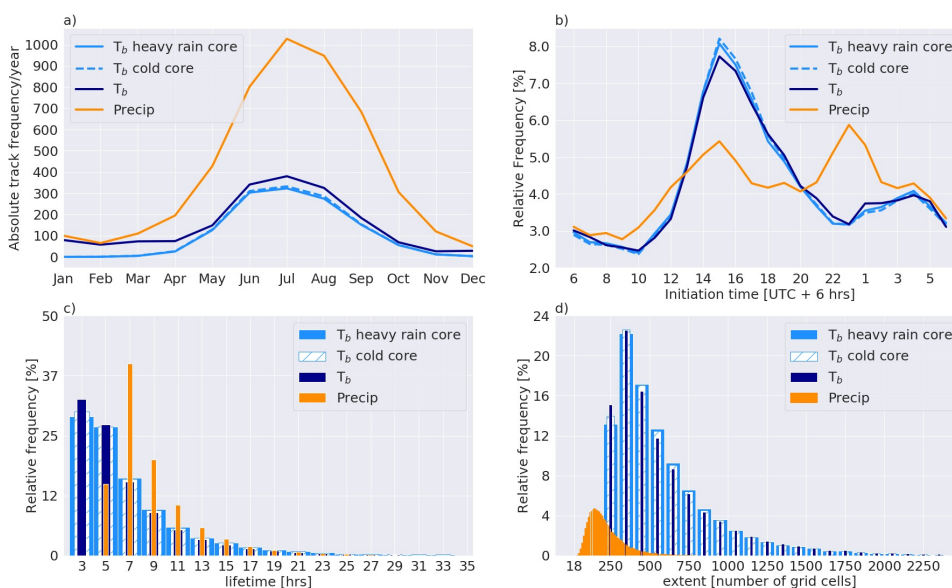


**Figure 5.** Comparison of characteristics for MCSs identified using four different tracking methods. The histograms show the a) annual cycle of tracks and the relative frequencies [%] for b) initiation time [UTC+6 hrs], c) lifetime [hrs] and d) mean extent [number of grid cells].

407 tive frequency of systems with spatial extents around the minimum area threshold (250  
 408 grid cells) is slightly higher for  $T_b$  than for  $T_b$  cold core and  $T_b$  heavy rain core, but all  
 409 three exhibit the largest frequency for systems between 350 and 500 grid cells (Fig. 5d).  
 410 This horizontal dimension corresponds to an area of about 80 000 km<sup>2</sup> and is thereby  
 411 close to the extent of a MCC (Maddox, 1980).

412 Contiguous precipitation cells are less common over high altitudes, which is shown  
 413 by the results of the *Precip* tracking over the TP that exhibits only a very small number  
 414 of cells despite the relatively small area threshold (Fig. 6a). The *Precip* tracking could,  
 415 for instance, miss MCSs that are initiated over the TP (e.g. through Tibetan Plateau  
 416 vortices (Curio et al., 2018)), but first grow into larger precipitation cells in the moister  
 417 downstream regions. Additionally, the biases of satellite-derived precipitation estimates  
 418 over high and complex terrain are only poorly understood, so it is unclear to which extent  
 419 the detection of contiguous precipitation is influenced by these (see more detailed  
 420 discussion in Section 4.2). Using precipitation only is therefore less useful to investigate  
 421 the role of weather systems originating over the mountains that result in organised convection  
 422 in the downstream regions. We conclude that the combined brightness temperature-  
 423 precipitation tracking ( $T_b$  heavy rain core) is clearly advantageous, because it can capture  
 424 a more complete cloud cell evolution and at the same time the precipitation evolution,  
 425 which is the most relevant parameter in a MCS.

426 The difference in total tracks between  $T_b$  and  $T_b$  cold core/ $T_b$  heavy rain core is  
 427 even more pronounced for the meso- $\beta$  tracking over the TP (Table 2), particularly during  
 428 the winter months (Fig. 6a). The seasonal cycle is clearly influenced by the higher  
 429 amounts of TCSs between January and April for  $T_b$  compared to  $T_b$  cold core/ $T_b$  heavy  
 430 rain core (Fig. 6a). A similar result was observed by Hu et al. (2017), who used MCS  
 431 data from the global *ISCCP Convective Tracking Database* (Wang et al., 2018) to ex-

432 amine convective systems over the TP. By filtering the tracked cloud features based on  
 433 an additional threshold for optical depth, they found that the winter maximum for MCS  
 434 events changed to a summer maximum, which is more consistent with the well-established  
 435 understanding of summer convection over the TP (Flohn & Reiter, 1968; Ye & Wu, 1998).  
 436 Hence, the seasonal cycle in Figure 6a shows the effect of falsely classified MCSs over the  
 437 mountains due to cold surfaces or cirrus clouds which was discussed earlier (see Section  
 438 2.1). When precipitation data is used to verify the presence of MCSs, we see a notable  
 439 reduction of such erroneous MCS classifications during the cold season. This is consis-  
 440 tent with the global dataset of Feng et al. (2021), who found a reduction of MCS tracks  
 441 over the TP by more than 50 %, when applying precipitation-based and brightness temperature-  
 442 based criteria compared to a tracking based on brightness temperatures only.

443 In addition, the results of the meso- $\beta$  tracking show differences in lifetime and spa-  
 444 tial extent between  $T_b$  and  $T_b$  cold core/ $T_b$  heavy rain core, where  $T_b$  results in gener-  
 445 ally more short-lived and smaller cells. This is also in line with our assumption that the  
 446 wrong cloud features or the background in the mountains are classified as MCSs, because  
 447 these are most likely less persistent than organised storm systems.

448 It is worth noticing that  $T_b$  cold core and  $T_b$  heavy rain core exhibit the same key  
 449 characteristics and almost the same number of monthly tracks in both the meso- $\alpha$  (Fig.  
 450 5) and the meso- $\beta$  tracking (Fig. 6). This means that most of the MCSs that develop  
 451 a rain core with  $> 5 \text{ mm h}^{-1}$  over at least 10 % of the minimum area at least once dur-  
 452 ing their lifetime also exhibit brightness temperatures  $< 200 \text{ K}$ . From this observation,  
 453 we conclude that the extra criterion for brightness temperatures that assures the devel-  
 454 opment of a convective core is enough to simultaneously assure that the system produces  
 455 heavy precipitation. Nevertheless, it remains advantageous to include precipitation data  
 456 in the tracking, in order to derive comparative information on the precipitation features  
 457 in the identified MCSs.

### 458 3.2 Spatial and temporal characteristics

459 As shown in Figure 7a, most of the TP + TPB systems are initiated in the east-  
 460 ern and southern TP. The Himalayas appear as a separator of MCS tracks, because the  
 461 low track density along the 3,000 m contour line in the south indicates that only few MCSs  
 462 can cross the mountain range. Instead, they are blocked by the orographic barrier and  
 463 produce rainfall over the Indo-Gangetic Plains and at the southern foothills of the Hi-  
 464 malayas, where a large amount of rainfall occurs (Kukulies et al., 2020). The same pat-  
 465 tern can be seen for TP + TPB west, but with generally smaller numbers of MCS tracks  
 466 over the TP (Fig. 7b). The highest initiation density of MCSs in the LE region are over  
 467 the Bay of Bengal for LE east (Fig. 7c) and over the Indian subcontinent for LE west  
 468 (Fig. 7d).

469 Figure 8 shows histograms of monthly occurrences (a), initiation time (b), lifetime  
 470 (c) and mean extent (d) for the MCS types LE west, LE east, TP + TPB west and TP  
 471 + TPB east. The total number of LE east and LE west are significantly higher than MCSs  
 472 that interact with the TP (TP + TPB). The maximum occurrence for LE east and TP  
 473 + TPB systems is in July, when the Indian summer monsoon season over the TP has  
 474 already started and matured, whereas LE west systems have their maximum in June (Fig.  
 475 8a). The MCS season for LE systems is generally more prolonged over the entire mon-  
 476 soon season with relatively high occurrences during May and October, where only very  
 477 few cases occur for TP + TPB (Fig. 8a).

478 An interesting feature of the diurnal cycle for MCS initiation is that TP + TPB  
 479 systems are mostly initiated in the afternoon and nearly never in the morning hours, whereas  
 480 LE west and LE east are initiated frequently during all hours and exhibit a smaller, less  
 481 pronounced afternoon peak (Fig. 8b). The second initiation peak during night that is  
 482 visible for the meso- $\alpha$  tracking (Fig. 5b), disappears in the meso- $\beta$  tracking (Fig. 6b),

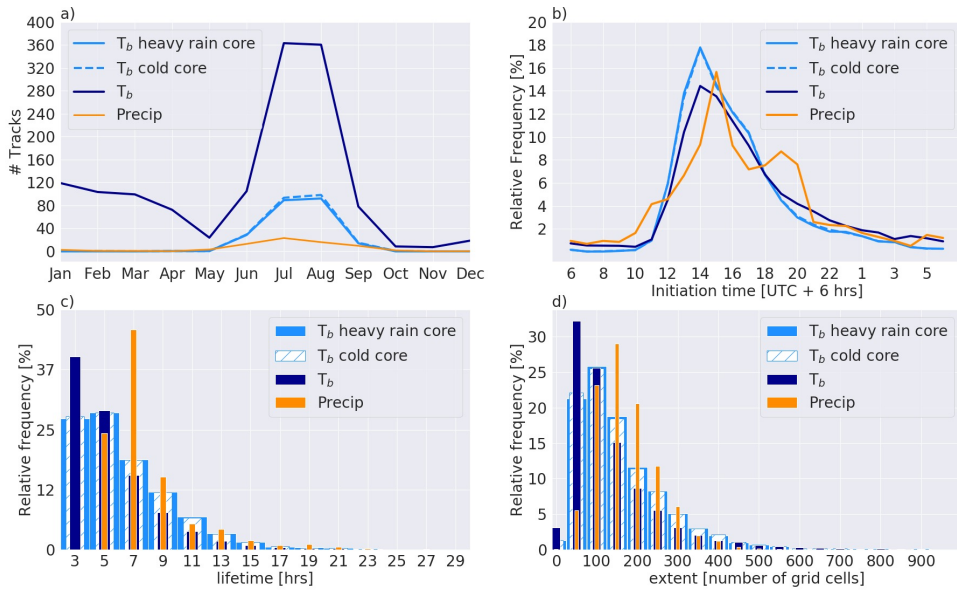


**Figure 6.** Same as in Figure 4, but for TCSs that were tracked by the meso- $\beta$  tracking (see Table 2 for criteria). *Precip* is from the same tracking as in Figure 4, but the characteristics are only shown for cells within the 3,000 m boundary of the TP.

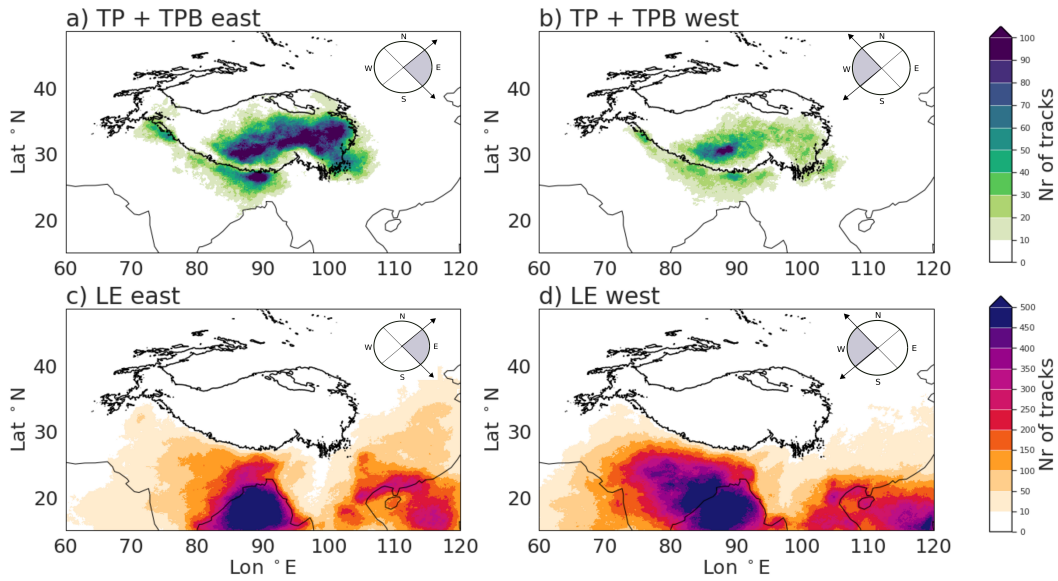


**Figure 7.** Density of initiation locations for TP + TPB east (a), TP + TPB west (b), LE east (c) and LE west (d). The colour shading shows the total number of MCS cloud features that were detected in each grid cell for the period 2000 to 2019. The grey region in the wind rose in each panel marks the directions that are covered by east-moving and west-moving systems. As shown in the wind roses, 'east' corresponds to directions between  $46^\circ$  and  $135^\circ$  and 'west' to directions between  $226^\circ$  and  $314^\circ$ .

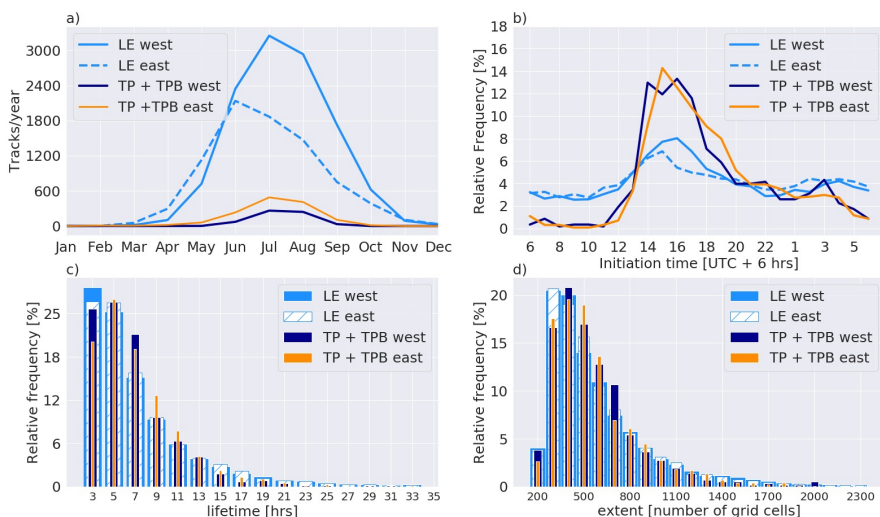


**Figure 8.** Spatial and temporal characteristics of eastward- and westward-moving MCSs in the LE and TPB regions. The histograms show the absolute occurrences of a) monthly tracks and the relative frequencies [%] for b) initiation time [UTC+6 hrs], c) lifetime [hrs] and d) mean extent [number of grid cells].

which suggests that the interaction with topography plays a crucial role for the initiation time. The distributions of lifetime and mean extent are similar for the four MCS types (Fig. 8c-d), showing that long-lived MCSs and large MCSs are not predominantly attributable to one of the four MCS types, but exist in each subgroup. More than 75 % of the tracked MCSs in each subgroup do not last longer than 12 hours, but all four MCS types also contain extreme cases with MCSs that last longer than 24 hours (Fig. 8c). The distribution of MCS extent is generally right-skewed, similar to the distribution of MCS lifetime, and MCSs with the most extreme extents belong to LE west and LE east (Fig. 8d). Most of the tracked MCSs have a mean extent between 300 and 600 grid cells, which corresponds to an area of about 60 000 – 120 000 km<sup>2</sup>. This shows that the area of the cloud shields for most of the systems is slightly larger than the required minimum cold area (Fig. 8d) and that the horizontal dimension of the dominating MCS type in the study area is comparable to *Mesoscale Convective Clusters* (described in Section 2).

It is important to understand the diurnal evolution of MCSs that originate over the TP, because they may be closely linked to topographically-driven diurnal flow patterns. Therefore, we further separate TP + TPB systems into MCSs that are initiated over the TP from systems that are initiated at lower elevations, but interact with the higher terrain (TPB), and compare the temporal evolution of these MCS types with the evolution of LE systems over land and ocean. Figure 9 shows histograms of the hours of the day at which the different MCS types are initiated (when they are first tracked as a cloud feature), reach maturity (the age of a cloud feature when its embedded area of precipitation > 5 mm h<sup>-1</sup> is greatest) and dissipate (when the area tracked as a cloud feature is last tracked). The first two histograms in Figure 9 refer to a) TP systems that are initiated at high altitudes and b) TCS that were tracked with the meso- $\beta$  tracking. These two MCS types show the same pattern with a distinct single maximum for initiation in the afternoon, maturity in the evening and dissipation during night. The resulting evening and night peaks in precipitation are consistent with the dominating di-

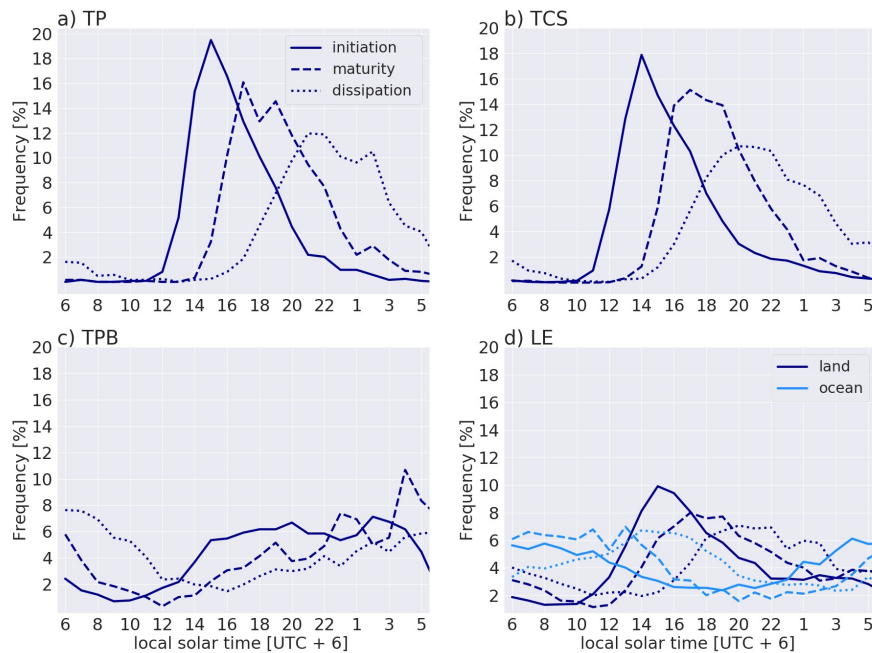


**Figure 9.** Temporal evolution of a) MCSs that initiated over the TP (1237 cases), b) TCSs (8580 cases) c) TPB (1537 cases) d) LE ocean (8096 cases) and LE land (15019 cases). The histograms show the relative frequencies for the times of the day associated with initiation, maturity (time point with maximum precipitation  $> 5 \text{ mm h}^{-1}$ ) and dissipation.

urnal cycle of precipitation over the southeastern TP (W. Xu & Zipser, 2011; Kukulies et al., 2019) and indicate that the diurnal flow has an important effect on mountain convection and the organisation of convective systems into larger systems. The main initiation, maturity and dissipation times for TPB systems exhibit, in contrast, a much larger range (Fig. 9c) with particularly high frequencies for both initiation and maturity during the evening and night hours. The resulting flatter diurnal cycle is more similar to MCSs initiated over the ocean (Fig. 9d), which are generally less affected by the diurnal forcing of surface heating over land. The less pronounced diurnal cycle of TPB systems indicates that the large-scale forcing (e.g. the monsoon flow that brings moist air to the mountains) is a more important factor than the diurnal circulation or that processes with different diurnal cycles lead to MCS formation at the edges of the TP. The high MCS initiation frequencies during night can, for instance, be related to downslope winds as a consequence of nighttime cooling in the Himalayas (Romatschke et al., 2010), whereas MCSs at the more eastern edges of the TP are influenced by other mechanisms. The second peak during night that occurred in the distribution for all MCSs (Fig.8b), can therefore be attributed to LE and TPB rather than to TP systems. LE systems over land have a similar but flatter diurnal cycle compared to TP and TCS (Fig. 9d), which suggests that the difference between LE and TP + TPB systems in Figure 8b is also caused by the large number of MCS tracks over the ocean (Fig. 7). These are not constrained by strong nocturnal cooling as in MCSs over land and can therefore continue to form and develop during the night (Houze, 2004; Huang et al., 2018).

### 3.3 MCS-associated precipitation

#### 3.3.1 Contribution to total and heavy precipitation

Figure 10 shows the average contributions of precipitation from tracked MCS cloud features to total precipitation and heavy precipitation (where heavy precipitation refers to rainfall events with a rate of at least  $5 \text{ mm h}^{-1}$ ) for each month during the monsoon season (May to September). During the onset of the Indian summer monsoon (May and June), the highest MCS contributions to precipitation are over the ocean (Bay of Bengal, Arabian Sea and South China Sea) and in the coastal regions, where MCSs bring more than 80 % of the total monthly precipitation (Fig. 10a-d). With the progression of the Indian summer monsoon, the MCS fraction of precipitation over the Bay of Bengal decreases to 40 to 60 % in September (Fig. 10i-j). Over land, there is a similar time evolution, with decreasing MCS fractions from the peak month in June. However, in contrast to the development over the Bay of Bengal, MCS contributions over the Indian subcontinent are higher in September than in May.

The regions over land with the highest MCS contributions are the Indo-Gangetic Plains and the Sichuan and Yangtze river Basins, where large areas exhibit more than 50 % MCS-associated rainfall, particularly during the mature phase of the monsoon between June and August (Fig. 10c-h). This regional pattern is consistent with Feng et al. (2021) who suggest that MCS contributions to total annual rainfall are highest over the Bay of Bengal (70 to 80%), above 50 % over large parts of the Indian subcontinent and between 30 and 40 % over most parts of China (Feng et al., 2021). These estimated ranges are very similar to our results which show only a few locations with slightly higher fractions, most likely because we focus on particular months during the monsoon season rather than on total annual precipitation.

In all months, the spatial pattern of MCS contributions is similar for both total and heavy precipitation, but most regions show a slightly higher MCS contribution for heavy precipitation (Fig. 10). The difference between the contributions to total and heavy precipitation is especially pronounced over the eastern parts of the TP (e.g. Fig. 10d, f, h). Over the TP, MCS contributions peak during July, where larger areas in the southern and eastern parts exhibit MCS fractions of 10 % and 20 % to total precipitation and 20 to 50 % to heavy precipitation (Fig. 10e-f). During June and August, the contribution of MCSs is below 20 % for most parts of the TP (Fig. 10c-d, g-h). In May and September, there is almost no MCS-associated precipitation over the TP, except for some small fractions at the eastern edges (Fig. 10a-b and i-j).

The results for the TP are also consistent with the estimations of Feng et al. (2021), but are in contrast with several previous studies that have suggested that MCSs over the TP can explain up to 70 % of the local precipitation during the warm season (Li et al., 2008; Hu et al., 2016). Given that Feng et al. (2021) have taken the same approach as we did, this result suggests once again that considering precipitation during MCS tracking can have a notable effect on conclusions about the role of MCSs in the regional water cycle in mid-latitude and alpine climate, where cold cloud tops are not necessarily linked with convective precipitation.

Another reason for the rather low MCS contributions over the TP in comparison with the surrounding downstream regions is the spatial extent of convective systems. In comparison with MCSs, TCSs (Table 2) make a significantly higher contribution to total and heavy precipitation over the high altitudes during the summer months (Fig. 11). These results confirm our hypothesis that precipitation-bearing systems that organize at smaller scales contribute to a larger extent to the total summer and heavy rainfall, highlighting these as an important component of the regional water cycle. Figure 11 shows the TCS contributions to total summer and heavy rainfall between June and August, when most of TCSs are detected (Fig. 6). As for the MCSs, the largest contributions

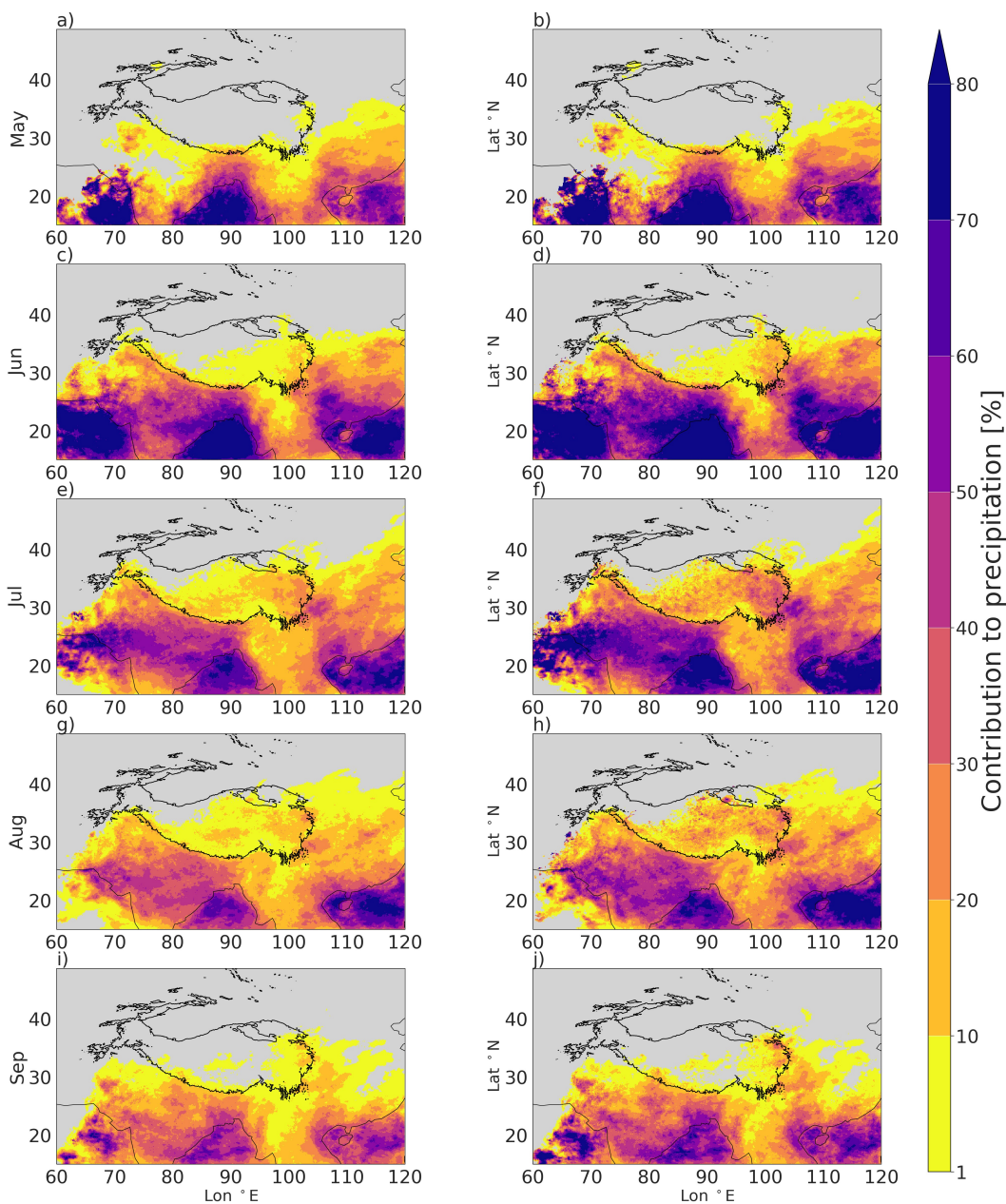


**Figure 10.** Maps of the monthly contribution of precipitation from MCSs, in % of total precipitation (a,c,e,g,i) and total heavy precipitation (b, d, f, h, j), which is the sum of precipitation produced by rain rates of at least 5 mm h<sup>-1</sup>. The subplots show each month between May and September for the period 2000 to 2019.

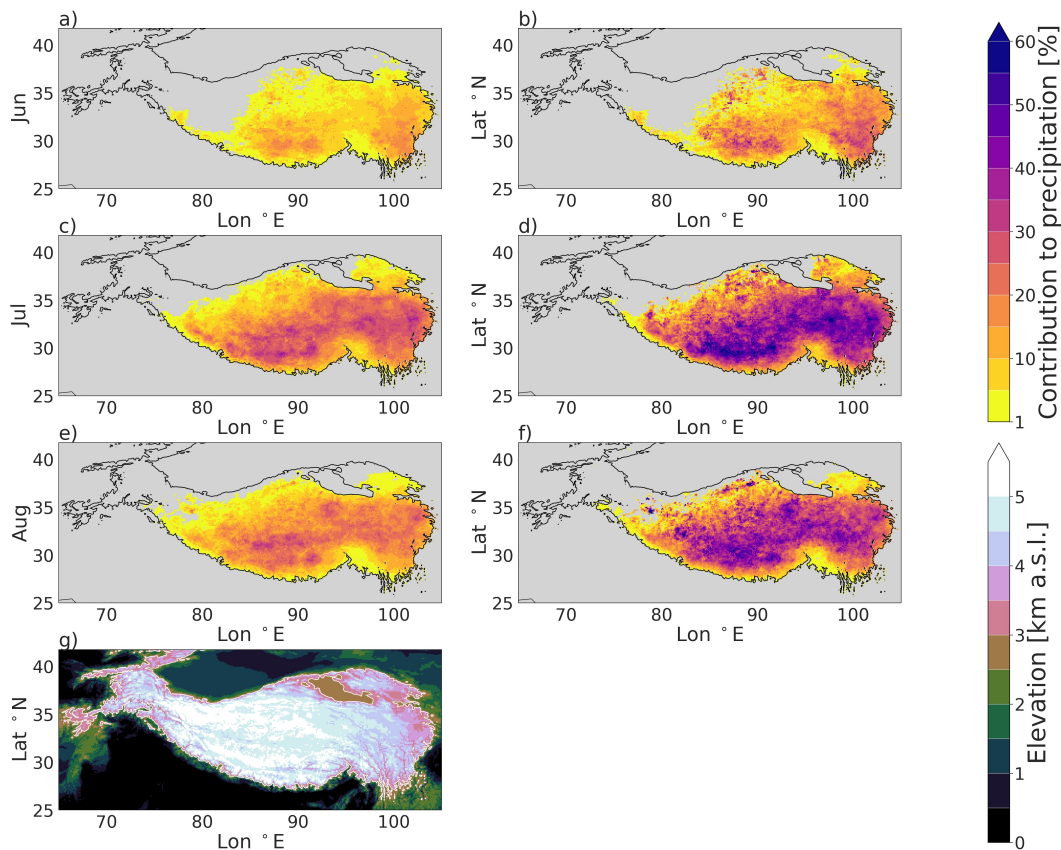


**Figure 11.** Same as in Figure 10, but for the smaller and more short-lived TCSs. These convective cells have approximately meso- $\beta$  dimensions in the horizontal plane (20 to 200 km). Contributions are shown for June to August as the ratio of precipitation from TCSs to total precipitation (a,c,e) and to total heavy precipitation (b,d,f). The elevation of the TP [km a.s.l.] is also shown for context (g).

582 to rainfall occur in July and August, where TCSs account for between 25 and 50 % of  
 583 the total precipitation over large areas of the central and eastern TP. Again, a strong  
 584 difference between the contribution to total and heavy precipitation is visible. The  
 585 contributions to heavy precipitation exhibit strong local maxima and therefore a  
 586 patchy spatial pattern with many grid cells in the southern and eastern TP for  
 587 which more than 60 % of local heavy precipitation is accounted for by tracked systems.  
 588 A large area of high values for the contribution occurs at the eastern edge of the TP (Fig.  
 589 11). This region is the same region that had the highest values for MCS contributions  
 590 over the TP (Fig. 10). There is no clear pattern linking the contribution to precipita-  
 591 tion with topography, but it should be noted that small-scale convective systems con-  
 592 tribute to summer precipitation even at elevations higher than 5,000 m a.s.l. (Fig. 11).  
 593 This means that organisation of convection over a few 10s of km is not necessarily con-  
 594 fined to the lower elevations over the eastern valleys of the TP.

### 595 3.3.2 Precipitation features

596 In the example snapshot in Figure 4, the convective core with heavy precipitation  
 597 is surrounded by a larger area of stratiform precipitation with moderate rain rates and  
 598 by an even larger area of non-precipitating clouds. Although stratiform cloud shields that

develop alongside MCSs may extend over large areas, the convective part of a MCS produces large amounts of rainfall over short periods and is therefore of higher environmental and hydrological relevance than the stratiform part. Figure 12 summarises the key characteristics of precipitation features in the MCSs that are associated with rain rates  $> 5 \text{ mm h}^{-1}$ , as an approximate differentiation for the more convective part of the MCS-induced rainfall. The precipitation features of MCSs in the TP + TPB are distinct from those in the LE region, because they have generally warmer cloud tops (Fig. 12a), less extreme rain rates (Fig. 12b) and smaller fractions of the total cloud area that is occupied by heavy precipitation (Fig. 12c).

As mentioned in Section 3.1, results from the different MCS tracking methods were similar, regardless of whether the  $T_b$  cold core or  $T_b$  heavy rain core criterion was applied (Table 2). This implies that MCS precipitation intensity is somewhat reflected in the observed mean brightness temperatures of the cloud features, because cloud cells that grow deeper during their lifetime have on average higher cloud tops (and hence colder brightness temperatures) and produce more intense precipitation. However, the relationship between brightness temperatures and precipitation intensification within a cloud is complex, and the pixels with the lowest temperatures do not usually correspond to the most convective part with heavy precipitation, but occur in the region where convection decays into cold stratiform clouds. Nevertheless, the general development of brightness temperatures during the MCS evolution is linked to precipitation intensity, so that the likelihood for extreme rainfall increases with colder cloud features (Klein et al., 2018). Therefore, the higher frequencies of low mean brightness temperatures and high rain rates in detected cloud features of the LE systems (Fig. 12a-b) suggest that MCSs that initiate and evolve over the plains are generally deeper and more intense systems than over the TP.

The distributions of the heavy rainfall area, expressed as a fraction of total cloud area, are right-skewed for all MCS types and show that for more than half of the identified MCSs, less than 25 % of the detected cloud area produces heavy precipitation (Fig. 12c). However, despite the small area such rain rates can produce substantial amounts of precipitation during short time periods, which is why the proportion of the total rainfall that is produced by higher rain rates shows a mirrored distribution for LE west and LE east. For the majority of these systems about 60 to 80 % of the total rainfall comes from heavy rain (Fig. 12d). This pattern is common for larger MCSs that have been found to produce around 40 % of stratiform and around 60 % of convective precipitation in other regions (Cheng et al., 1979; Rutledge et al., 1979). Indeed, for TP + TPB, the proportion of heavy rainfall instead exhibits a large range of values, which confirms again that most of the MCSs over and in the vicinity of the TP are not as well-developed as the MCSs in the downstream regions.

### 3.3.3 Heavy impact MCSs

The total rainfall amount produced by a MCS depends on the system's lifetime, size and intensity. The four MCS types presented in Figure 8 include MCSs with highly variable track characteristics. Thus, we further divide each MCS type into three categories, according to lifetime, size and intensity. To identify what characterises MCSs with a potentially heavy impact compared to MCSs that produce smaller amounts of precipitation, these MCS classes are examined with respect to the total amount of heavy precipitation they produce during their lifetime (Fig. 13). Figure 13 shows the distributions of total heavy precipitation (from rain rates  $> 5 \text{ mm h}^{-1}$ ) for the four MCS types divided into the three classes of lifetime, size and intensity.

The boxplot shows that the total amount of heavy precipitation varies substantially between the tracked MCSs. Differences between the total heavy precipitation distributions for the five previously defined MCS types (LE west, LE east, TP + TPB west, TP

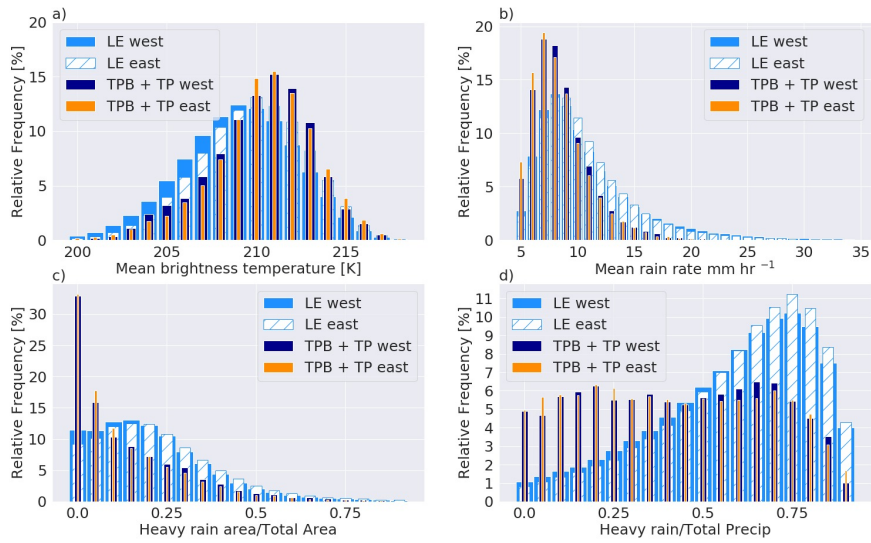


**Figure 12.** Characteristics of detected MCS cloud features that contain heavy rainfall (here defined as rainfall  $>5 \text{ mm h}^{-1}$ ). The histograms show the a) mean brightness temperatures [K], b) mean rain rate [ $\text{mm h}^{-1}$ ], c) the proportion of the area with heavy rainfall in relation to the total cloud area and d) the amount of heavy rainfall in relation to total rainfall in the individual precipitating cloud features.

+ TPB east and TP) are mainly between LE and TP + TPB types, which supports our earlier finding that the genesis location (plains or mountains) is more important for the key characteristics and total amount of heavy precipitation than their respective propagation directions. Hence, both eastward- and westward-moving MCSs over lower and higher elevations may produce substantial amounts of heavy rainfall, but MCSs initiated over the TP or around its boundary are generally smaller and include less frequent extreme cases. Comparing lifetime, area and intensity for systems in the different categories, the most pronounced difference in total heavy rainfall is visible between systems that last longer than 24 hours and systems that are shorter-lived (Fig. 13a). The mean, maximum and outliers for the distributions of total heavy precipitation also increase as the area covered by the system increases (Fig. 13b). However, the effect of the area is stronger for LE systems than for TP + TPB (Fig. 13b). The total heavy precipitation is less obviously related to the temperature of the coldest (most convective) part of the system (Fig. 13c).

MCSs that are initiated over the TP are located in the lowest-precipitation range of the distribution for each category, which means that those systems produce the smallest amounts of heavy precipitation. This is related to the fact that the extreme categories with the highest lifetimes and largest extents only contain very few TP cases and that none of the TP cases had a cloud feature  $< 200 \text{ K}$  that extended over an area of  $50,000 \text{ km}^2$ . The MCS example case from July 2008 (Fig. 4) is also marked in Figure 13 (red cross). This MCS belongs to the TP + TPB east type and produced more heavy precipitation than most other TP + TPB systems. It falls into the largest category for mean extent, but produced less total heavy precipitation than LE systems in same extent category (Fig. 13a-b). The example MCS case also produced less total precipitation than most of the other TP + TPB east systems that persisted for more than 24 hours (Fig.

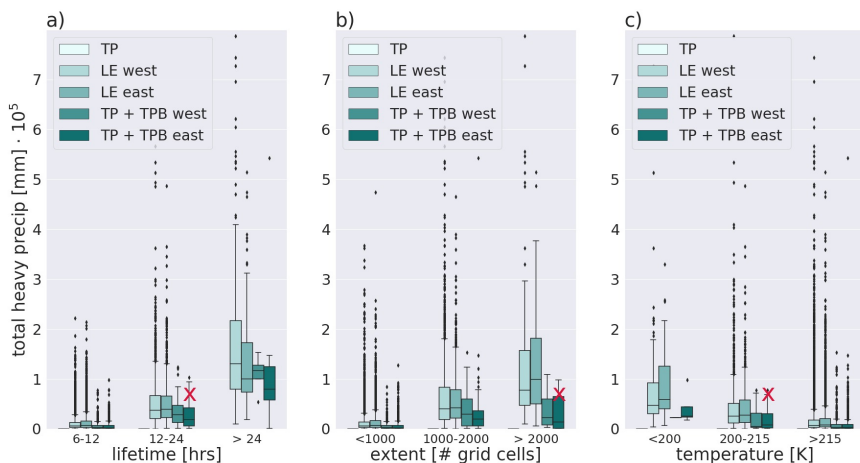


**Figure 13.** Boxplot showing the distribution of total heavy precipitation produced by eastward- and westward-moving MCSs which are initiated over the TP (TP), stay within or cross the TP (TP + TPB) and remain in the surrounding lower-elevation plains (LE). MCSs are divided into different classes depending on a) lifetime [hrs], b) extent [number of grid cells] and c) temperature [K]. The temperature refers to the lowest brightness temperature for a contiguous area within the cloud feature. The red cross highlights the MCS from of July 2008 used as a case study (see Section 2).

13a-b). This means that many detected MCS cases produce larger amounts of total heavy precipitation, which shows that MCSs with a similar potential impact occur frequently and pose a serious risk for the region they hit.

Figure 14 shows the joint frequency distributions for total heavy precipitation and maximum rain rate (a), minimum brightness temperature (b), system lifetime (c), and maximum area (c) of the MCSs that produce more than the 95<sup>th</sup> percentile of precipitation. This helps understanding the relationship between MCS characteristics and total heavy precipitation for heavy impact MCSs and shows, for instance, that the most intense rain rates or coldest brightness temperatures are not necessarily found in the systems that produce most heavy precipitation (Fig. 14a-b). Although none of the four characteristics stands out as a major controlling factor for the total heavy precipitation produced by the system, the joint frequencies show clearly that lifetime and maximum area have a greater effect than the intensity of rain rates or brightness temperatures. Hence, a MCS is more likely to produce large amounts of heavy precipitation the longer it persists and the larger it grows (Fig. 14c-d).

### 3.4 Large-scale atmospheric environments

The different characteristics between MCSs that interact with the topography of the TP compared to MCSs in the LE region are also reflected in the large-scale atmospheric environments that are associated with the respective MCS types. In Figures 15 to 18, we compare large-scale composites of the tracked MCSs, composed as the 6-hour mean prior to their initiation stages. To describe the large-scale atmospheric conditions, we use mid-/upper-level wind circulation, atmospheric moisture transport and convective available potential energy (CAPE) taken from the ERA5 reanalysis (Hersbach et al., 2020). The composites are shown as anomalies which were computed by subtract-

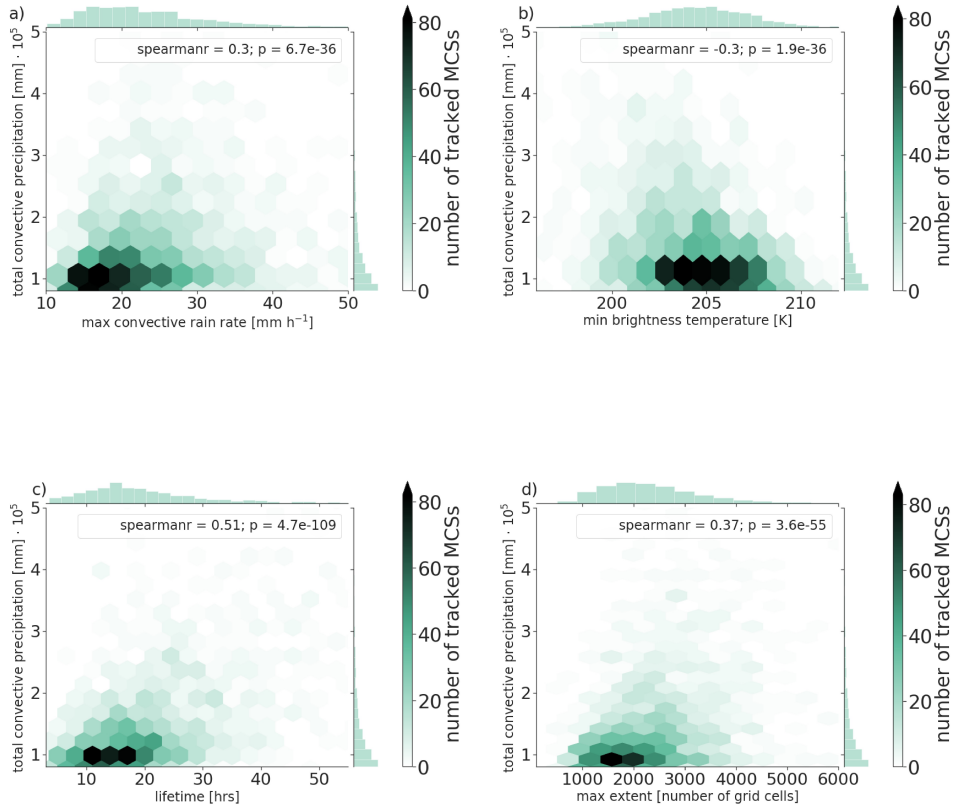


**Figure 14.** Joint frequency distributions for total heavy precipitation and a) maximum rain rate  $> 5 \text{ mm h}^{-1}$ , b) minimum brightness temperature [K], c) lifetime [hrs] and d) maximum area of precipitation  $> 5 \text{ mm h}^{-1}$  [number of grid cells] for the MCS that produce more than the 95<sup>th</sup> percentile of total integrated rainfall from rain rates above  $5 \text{ mm h}^{-1}$ . The colour scale indicates the number of identified MCS tracks which correspond to the values shown in the joint space. The histograms on the x and y axes show the individual frequencies of each variable.

699 ing the summer climatology 2000 to 2019 (displayed in the lower panels) from the com-  
700 posite mean. Positive anomalies indicate hence that the respective variable exhibits higher  
701 values for the MCS composite compared to the summer mean. We focus on the six hours  
702 prior to the first MCS detection, in order to examine synoptic patterns which may favour  
703 the initiation at a stage where no feedback of the MCSs to the large-scale environment  
704 has been introduced yet. Given the large number of MCSs with different intensities dur-  
705 ing the past two decades, the composite analysis focuses on MCSs that belong to the 95<sup>th</sup>  
706 percentile for values of total MCS-induced precipitation (as in Fig. 14). Bearing in mind  
707 that various large-scale circulation processes may favour the initiation of convection in  
708 the diversified downstream regions, two major regions of MCS initiation in the LE are  
709 inspected (Fig. 7): over the Bay of Bengal (BOB) and over China.

710 We look at the upper-level dynamic forcing which is particularly important for the  
711 TP, where most locations have surface pressures close to 500 hPa. The 200 hPa zonal  
712 wind serves as a proxy for the strength and location of the subtropical westerly jet (Schiemann  
713 et al., 2009), which in turn is influenced by the anticyclonic circulation around the South  
714 Asian High (with large parts of its main body located over the Iranian and Tibetan Plateau).  
715 Previous studies have shown that intense rainfall events over South-East Asia are often  
716 linked to anomalous water vapor transport and upper-level circulation caused by sub-  
717 seasonal variations of the South Asian High movement and intensity (Jia & Yang, 2013;  
718 Ren et al., 2015; Shang et al., 2019). In addition, we look at the 500 hPa geopotential,  
719 as an indicator for horizontal pressure gradients over the South-East Asian continent and  
720 low-level circulation over the TP.

721 A prominent large-scale feature for MCSs that are initiated over the TP and TCSs  
722 is the intensification of the westerly jet, which is visible through the positive anomaly  
723 in the 200 hPa zonal wind over the northern TP and the simultaneous negative anomaly  
724 south of the major jet axis (Fig. 15a-b), which is located around 40°N in the climatol-  
725 ogy (Fig. 15f). Schiemann et al. (2009) have highlighted that the intensification and north-  
726 ward shift of the westerlies from June onward are associated with a strong Indian sum-  
727 mer monsoon circulation and hence increased moisture supply and diabatic heating over  
728 the TP. Moreover, Li et al. (2014) found that the westerly jet can favour cyclonic rota-  
729 tion south of its maximum speed through upper-level divergence and convergence close  
730 to the surface over the TP. The anticyclonic circulation of the South Asian High is man-  
731 ifested through the positive anomalies in upper-level zonal winds and shows also a promi-  
732 nent intensification for TP and TCS (Fig. 15 a-b). This is consistent with Lai et al. (2021),  
733 who showed that the South Asian High played a crucial role in controlling the season-  
734 ality of TP precipitation in anomalously wet years. TPB, LE BOB and LE China show  
735 the inverse pattern with a weaker anticyclonic circulation (Fig. 15c-e).

736 The strong positive upper-level zonal winds south of the TP and the southerly shift  
737 of the westerly jets for MCSs over China (Fig. 15e) are accompanied by an intensified  
738 horizontal pressure gradient at 500 hPa (Fig. 16e). Similar to LE BOB (Fig. 16c), but  
739 in contrast to TP and TCS (Fig. 16a-b), LE China shows a strong decrease in geopo-  
740 tential northeast of the TP, which suggests a strong upper-level wind forcing due to the  
741 enhanced north-south gradient in pressure (Fig. 15e).

742 All MCS types are clearly connected to anomalies in atmospheric water vapor trans-  
743 port to the respective regions of MCS genesis (Fig. 17a-e). It is noticeable that the mois-  
744 ture transport from the Bay of Bengal towards the mountain regions is enhanced for TP  
745 and TCS (Fig. 17a-b) and that the main region of this positive atmospheric water va-  
746 por transport south of the Himalayas exhibits in contrast negative anomalies for TPB,  
747 LE BOB and LE China (Fig. 17c-e). Whereas the Southern ocean is the key moisture  
748 source for TP, TCS and LE BOB, TPB and LE China are associated with negative anoma-  
749 lies over the Arabian Sea and Bay of Bengal (Fig. 17c,e). This suggests that most of the  
750 moisture for MCSs that are initiated over China comes from the continent and from the  
751 South China Sea.

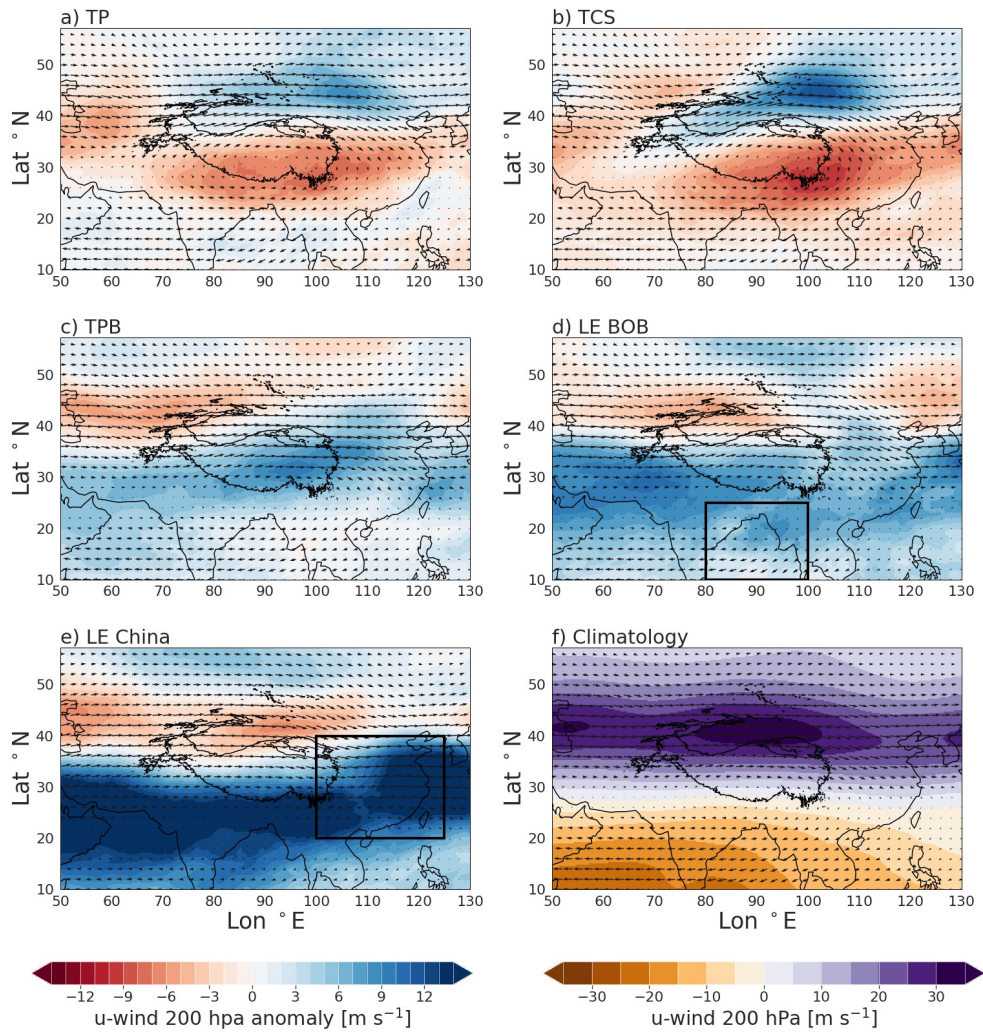


**Figure 15.** ERA5 composite maps for 200 hPa wind circulation composed as the mean of six hourly time steps prior to the initiation stages of different MCS types: a) TCS, b) TP, c) TPB, d) LE BOB and e) LE China. The shading shows the anomaly of the zonal wind component at 200 hPa, computed as the composite mean minus the climatology for June to August for the period 2000 to 2019 (shown in panel f).

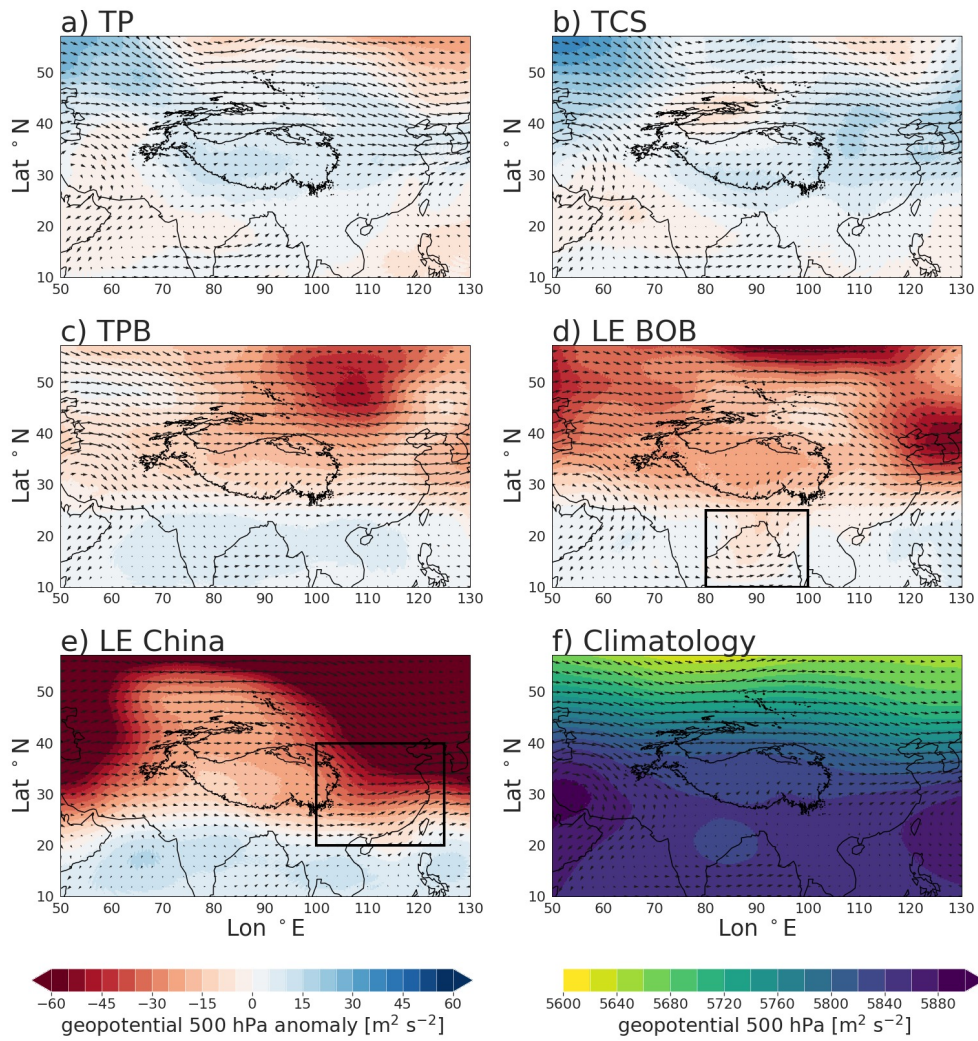


**Figure 16.** Same as in Figure 15, but for 500 hPa wind circulation. The shading indicates shows the anomaly of the 500 hPa geopotential height.

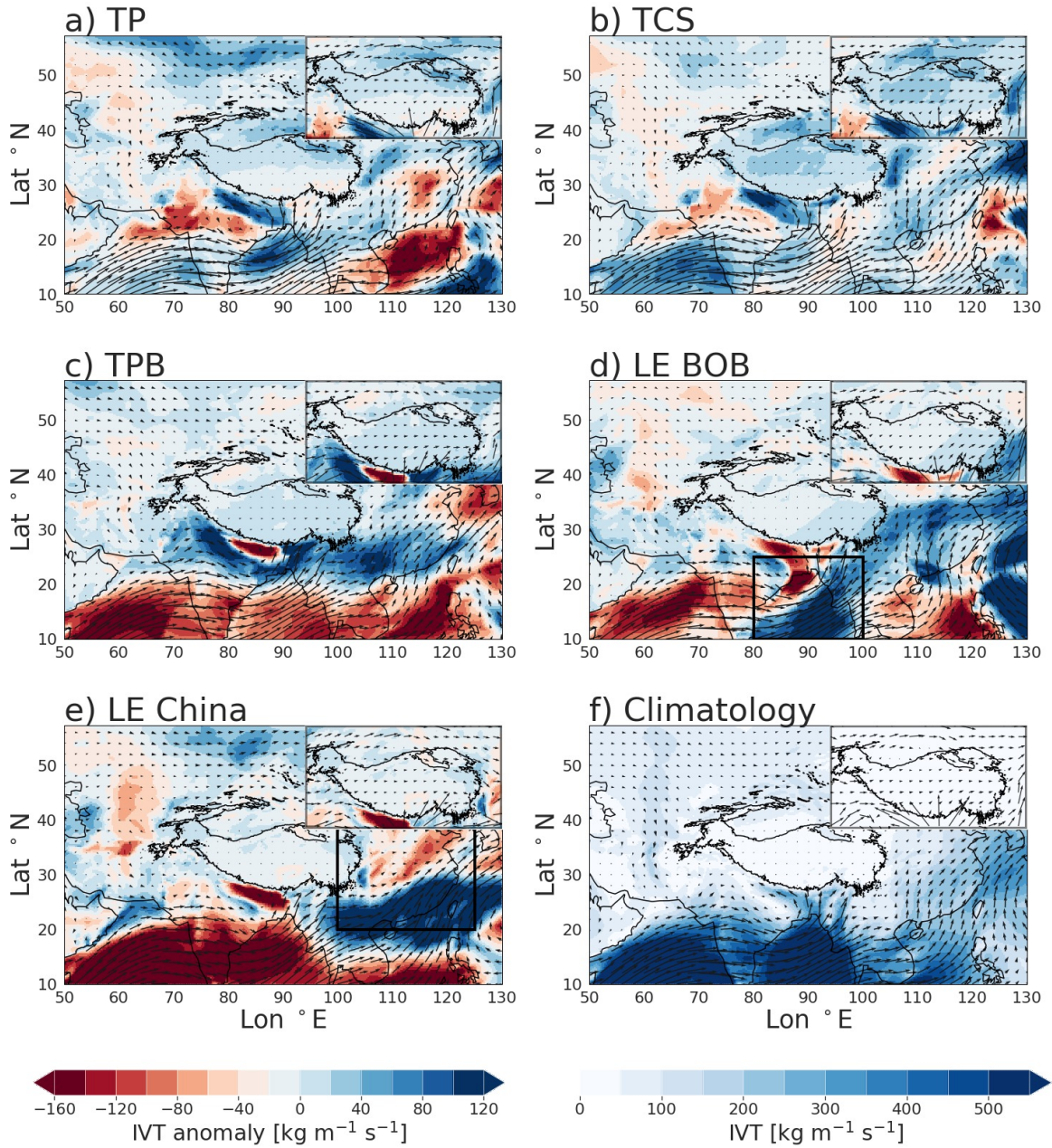


**Figure 17.** Same as in Figure 15, but for vertically integrated water vapour transport. The arrows are the vectors of the vertically integrated water vapour fluxes ( $q_u$  and  $q_v$ ) and the shading is the anomaly in total vertically integrated water vapour transport (IVT), defined as  $\sqrt{q_u^2 + q_v^2}$ . The top right figure is a zoomed in image of the TP using a multiplying factor of 1.5 to show more clearly from which direction the water vapour advects.

752 In addition to the large-scale wind forcing and sufficient moisture supply, a key fac-  
753 tor for organised convection is atmospheric instability, which is indicated by CAPE (Fig.  
754 18). Figure 18a shows a strong positive anomaly in CAPE over the TP and in the down-  
755 stream regions east of the TP (over Mainland China), when MCSs are initiated over the  
756 TP. The same is true for TCSs, where the positive CAPE anomaly over the central TP  
757 is even stronger (Fig. 18b). The accumulation of CAPE appears as an important fac-  
758 tor for convection initiation over and close to the mountains, because these regions ex-  
759 hibit on average CAPE values below  $400 \text{ J kg}^{-1}$  (Fig. 18e), which is not sufficient to de-  
760 velop severe storms (Kirkpatrick et al., 2011). Furthermore, the positive CAPE anom-  
761 alies over the TP and in the downstream regions to the east occur simultaneously with  
762 a strong negative CAPE anomaly at the Indian east coast (Fig. 18a-b). TPB systems  
763 do not show the same positive anomaly over the TP, but instead positive anomalies over  
764 the ocean and the South Asia (Fig. 18c). The bimodal ocean-land pattern that was vis-  
765 ible for TP and TCS is the inverse for LE BOB, where a strong negative CAPE anomaly  
766 over Mainland China occurs simultaneously with a strong positive CAPE anomaly over  
767 the MCS genesis region, the Bay of Bengal (Fig. 18d). The fact that the average con-  
768 ditions during summer exhibit large amounts of CAPE ( $> 1800 \text{ J kg}^{-1}$ ) over the ocean  
769 (Fig. 18e) shows that the accumulation of CAPE is a particularly important factor for  
770 MCSs over and east of the TP, because a stronger dynamical and thermodynamical forc-  
771 ing is needed for convective storms to develop. Given that the high MCS frequency over  
772 the Bay of Bengal and Indian subcontinent (Fig. 7), this means that convection can more  
773 frequently develop in these regions even with weaker dynamical and thermodynamical  
774 disturbances. Other hotspot regions for convective storms also show that environments  
775 with high average CAPE values require smaller anomalies for storms to develop, for in-  
776 stance the U.S. Great Plains where CAPE anomalies are substantially smaller during  
777 summer compared to spring (Song et al., 2019).

778 The fact that MCS initiation over the TP (TP and TCS) is related to enhanced  
779 moisture transport, a more intense upper-level jet and anticyclonic circulation as well  
780 as strong positive CAPE suggests that stronger dynamic and thermodynamic pertur-  
781 bations are needed to initiate larger MCSs over on the leeside of the mountains. The pos-  
782 itive CAPE anomaly to the east of the TP also shows that the synoptic conditions favour-  
783 ing MCS initiation over the TP could potentially lead to extreme events when the ac-  
784 cumulated CAPE in the eastern downstream regions is released.

## 785 4 Discussion

### 786 4.1 Role of MCSs in precipitation

787 Previous studies have highlighted MCSs as the main source of summer precipita-  
788 tion over the TP. Here, we argue that it is important to take the scale of convection into  
789 account, when drawing conclusions about as MCSs as a component of the regional wa-  
790 ter cycle of the TP. Our results show that larger MCSs are a main component in the wa-  
791 ter cycle in the LE region, whereas small-scale convection is a more important source  
792 of precipitation over the TP. The reasons for discrepancies in total MCS numbers and  
793 MCS-associated precipitation between previous studies and our findings is three-fold. Firstly,  
794 our method for MCS tracking is less likely to include cirrus clouds or cold surfaces be-  
795 cause we assure that cloud cold tops are also associated with a heavy rain core. Secondly,  
796 our method for calculating MCS-associated precipitation differs from commonly used meth-  
797 ods. Many studies use a radius approach, where all precipitation within a certain radius  
798 of the MCS centre is considered to be MCS-induced precipitation, instead of tracking  
799 precipitation features within cloud cells as we have done here. Our results show that the  
800 area with heavy precipitation of some MCSs can vary significantly (Fig. 12), and the method  
801 we have developed here could therefore give a more accurate estimate of precipitation  
802 associated with a MCS, which is most likely dependent on the size of the MCS. Addi-  
803 tionally, our calculated MCS contributions to precipitation are consistent with those es-

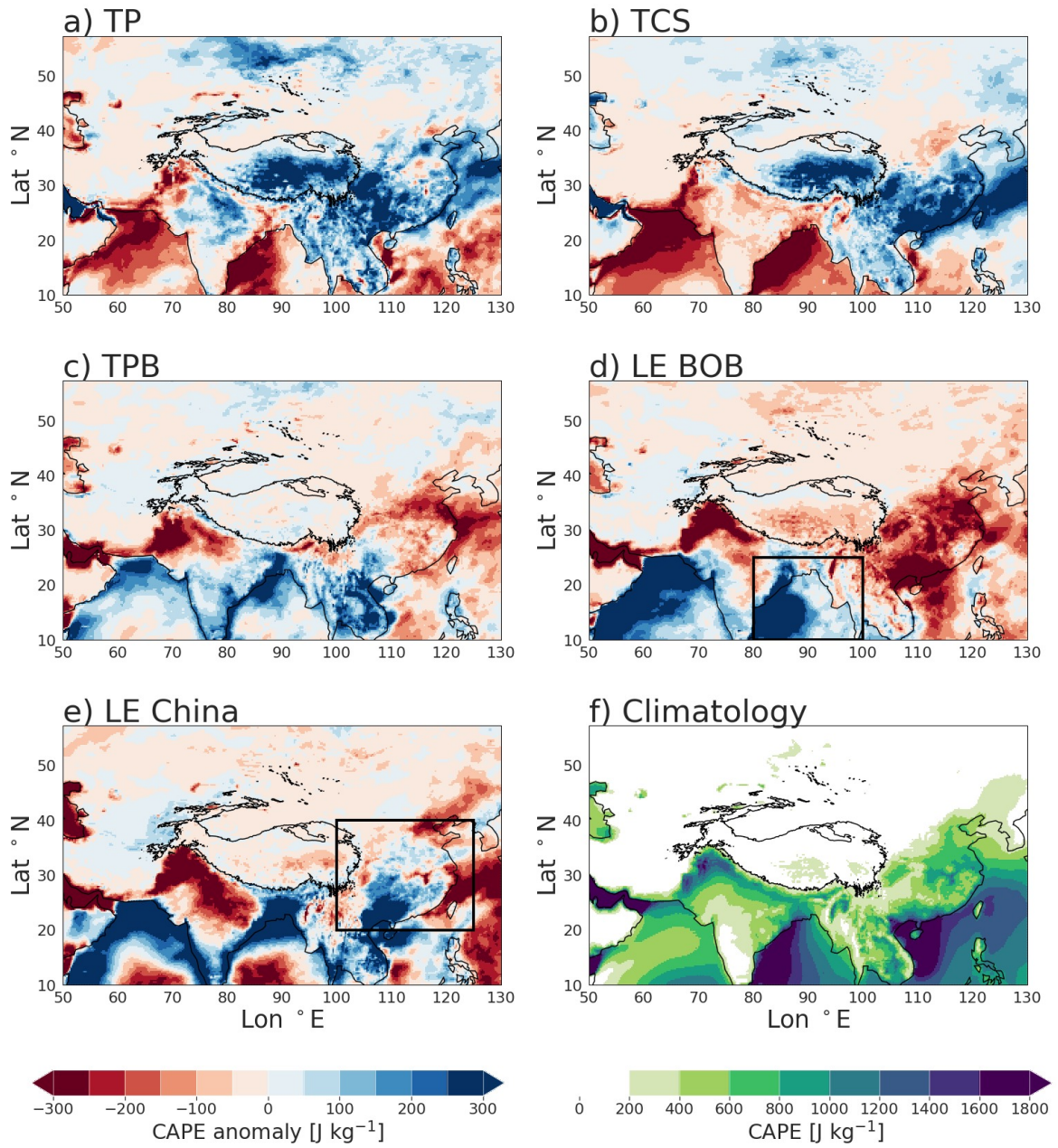


**Figure 18.** Same as in Figure 15, but for the anomalies in convective available potential energy (CAPE).

804 timated by Feng et al. (2021), who use a similar method for MCS tracking and precip-  
805 itation attribution. Thirdly, we demonstrated that the number of tracked MCSs over the  
806 higher altitudes is very sensitive to the area threshold and that meso- $\beta$  convective sys-  
807 tems have higher contributions to total summer and heavy precipitation over the TP than  
808 meso- $\alpha$  systems (with similar dimensions as MCC (Maddox, 1980)).

809 The MCS contributions to heavy precipitation (Fig. 10b, d, f, h, j; Fig. 11b, d, f)  
810 revealed that there is heavy precipitation over the TP that could not be associated with  
811 the tracked cloud clusters. This suggests that convective modes that are not targeted  
812 by our tracking algorithm, such as isolated thunderstorms and deep convection, also play  
813 a significant role for summer precipitation. A similar conclusion was drawn by Houze  
814 et al. (2007) who investigated deep convective features based on Tropical Rainfall Meas-  
815 uring Mission (TRMM) Precipitation Radar (PR) data and found that deep convective  
816 echoes occur over the TP in a scattered manner, whereas more prominent mesoscale con-  
817 vective features organised along the Himalayan ranges. Possible explanations for the dom-  
818 inance of isolated convective cells instead of organised convection could be the highly vary-  
819 ing topography that act as mechanical barriers, limited moisture supply and cirrus clouds,  
820 which may locally inhibit convective heating over some parts during summer (Roebber  
821 et al., 2002). The simultaneous occurrence of cirrus clouds and convective clouds, as re-  
822 vealed in the bimodal cloud top height distribution over the TP during summer (Chen  
823 et al., 2018; Kukulies et al., 2019), suggests that the effect of cirrus clouds is not neg-  
824 ligible.

825 According to the definition used here, MCSs with meso- $\alpha$  dimensions were occa-  
826 sionally found over the TP (in total 1237 cases over 20 years). These are associated with  
827 heavy precipitation between late afternoon and early evening (Fig. 9a) and have the high-  
828 est contributions to heavy precipitation in the eastern parts of the TP (Fig. 10d,f,h). Al-  
829 beit the total amount of heavy precipitation produced by these MCSs was relatively small  
830 compared to that from MCSs over the Indo-Gangetic Plain and along the Indian coast  
831 (due to generally lower intensity and lifetimes). However, these MCSs can still be very  
832 destructive, in particular when they do not move far and produce instead a lot of rain-  
833 fall over the same populated area, like in the case that was shown in Section 3.1 that lead  
834 to severe flooding in the Sichuan basin (Feng et al., 2014). Because such MCSs are par-  
835 ticularly hazardous, future projections for both MCS frequency, intensity, and also their  
836 likelihood to occur as quasi-stationary or back-building types are needed.

837 The importance of MCSs for summer mean and heavy rainfall was significantly higher  
838 in most of the LE region south of the Himalayas than over the TP. Densely populated  
839 regions south of the Himalayas and in the Indo-Gangetic Plain experience frequent MCS  
840 events, which produce substantial rainfall amounts due to their longevity and large size.  
841 Feng et al. (2018) found that long-lived MCSs over the Great Plains in the USA pro-  
842 duced 2–3 times more precipitation than short-lived MCSs. A similar result was found  
843 in this study, where both mean and maximum total heavy precipitation of MCSs that  
844 persisted longer than 24 hours were about twice as high as MCSs that persisted between  
845 12 and 24 hours and four times higher than MCSs that persisted for up to 12 hours. The  
846 fact that the differences in MCS contributions to total vs. total heavy precipitation were  
847 relatively small in the LE region, shows that MCSs in the LE region are not only an im-  
848 portant factor for local extremes, but also a significant component in the water cycle.  
849 Hence, changes in MCS patterns do not only affect the risk of severe weather for pop-  
850 ulated regions, but can also lead to changes in the accumulated rainfall during one sea-  
851 son and thereby affect crop yields and water resources.

852 It should be noted that the contribution of MCSs to precipitation may have been  
853 underestimated in the downstream regions, because our MCS tracking method was opti-  
854 mised for the TP. Since cloud top temperatures for deep convective cells of the same  
855 depth are higher over lower-elevation regions than the TP, an improvement of MCS track-  
856 ing for these regions could be achieved by considering the difference of cloud top tem-

857 peratures to local surface temperatures rather than applying one brightness tempera-  
858 ture threshold over different altitudes. Additionally, the used data product GPM IMERG  
859 may underestimate very high rain rates, which will be discussed in more detail in the next  
860 section.

#### 861 4.2 Retrieval uncertainties

862 The results of this paper suggest that the role of MCSs in precipitation can be il-  
863 luminated by utilising high-resolution precipitation datasets like the newly available GPM  
864 IMERG v06 in combination with IR imagery from geostationary satellites. This is a way  
865 to reduce uncertainties related to IR brightness temperatures, especially if the region of  
866 interest includes various surface types and complex topography. Nonetheless, one should  
867 also be aware of the uncertainties related to satellite precipitation retrievals, particularly  
868 over high terrain.

869 Three specific aspects of uncertainty are related to snowfall detection, the under-  
870 estimation of warm orographic rain and the underestimation of intense convective pre-  
871 cipitation. It has repeatedly been shown that the inclusion of Dual-Frequency Precip-  
872 itation Radar (DPR) in GPM IMERG exhibits improved capabilities for snowfall detec-  
873 tion both over the TP (Ma et al., 2016) and in other mountain regions (Wen et al., 2016).  
874 Spaceborne radar observations can significantly improve rain retrievals from IR and mi-  
875 crowave observations, because the active radar sensors can more accurately derive the  
876 precipitation phase. Additionally, radar reflectivity is more directly linked to surface pre-  
877 cipitation intensity than passive microwave observations, which infer rain rates based on  
878 ice scattering aloft. However, radar sensors such as DPR have a lower spatial coverage  
879 and over snow surfaces, the input data for the IMERG retrieval are only obtained from  
880 passive microwave sensors. This can lead to erroneous snowfall estimations and to wet  
881 biases due to falsely detected precipitation events as a consequence of increased scatter-  
882 ing at the surface. At the same time, warm orographic precipitation may be underes-  
883 timated in regions with highly complex topography, because of low IR brightness tem-  
884 perature signatures and absent ice scattering, which is crucial for precipitation detec-  
885 tion by passive satellite sensors. The GPM IMERG retrieval may also underestimate very  
886 intense hourly rain rates. In a comparison between IMERG and a ground-radar network  
887 over the US, it has, for instance, been shown that the occurrence frequencies of convec-  
888 tive rainfall in MCSs (here defined as  $> 10 \text{ mm h}^{-1}$ ) were significantly underestimated  
889 by IMERG in all seasons with the strongest bias during the summer season (Cui et al.,  
890 2020). This is also true for smaller isolated cells of deep convection, because the spatial  
891 averaging of reflectivities at the resolution of the precipitation radar can lead to a sig-  
892 nificant underestimation of the rain rates in such systems (Duan et al., 2015).

893 An additional point is that sensor- and retrieval-related biases can only to a very  
894 limited extent be corrected by gauge calibration, because meteorological stations in the  
895 TP region are sparsely distributed and mainly located in the valleys. Even though it has  
896 been shown that GPM IMERG reduces the well-known wet bias of total and seasonal  
897 mean precipitation over the TP (Xu et al., 2017; Zhang et al., 2018), the uncertainties  
898 in subhourly and hourly precipitation have not been sufficiently studied. The evaluation  
899 of satellite precipitation estimates against in-situ observations is necessary to better un-  
900 derstand various biases that can occur in high and complex terrains and this has not ex-  
901 tensively been done over the TP. Systematic validation studies such as Cui et al., (2020)  
902 are therefore needed to quantify the effect of various biases on MCS feature detection  
903 and tracking before MCS datasets can be used for hydrological applications.

904 Given the above-named uncertainties, the absolute values of retrieved rain rates  
905 should be interpreted with caution, because especially the higher rain rates (e.g.  $> 5 \text{ mm}$   
906  $\text{h}^{-1}$ ) and consequently the total accumulated precipitation of one MCS may be under-  
907 estimated in this study. Nevertheless, GPM IMERG provides robust information whether

908 or not contiguous areas of relatively higher rain rates are present. Therefore, we think  
909 that it is a useful dataset to examine the main features of precipitation within MCSs in  
910 a comparative way. To get a more complete understanding of different convective modes  
911 and their precipitation features over the TP, further studies should also consider the ver-  
912 tical structure of the organised convective cells.

### 913 4.3 Possible mechanisms for MCS formation

914 This study provides an observational perspective on MCSs over a larger region, where  
915 multiple processes may lead to the organisation of convection at the mesoscale. Most of  
916 the MCSs in the LE region over land were found south of the TP, over the Indo-Gangetic  
917 Plain and close to the Himalayas, as well as over the southern Indian subcontinent and  
918 at the coast of the Bay of Bengal. Both land and ocean south of the TP are influenced  
919 by frequent monsoon low pressure systems during the wet season, and these have been  
920 associated with barotropic instabilities that may be amplified by wind-moisture feedbacks  
921 (Boos et al., 2017; Diaz & Boos, 2019). Because we do not explicitly exclude tropical cy-  
922 clones and monsoon low pressure systems, the high track densities over the Indian sub-  
923 continent and ocean (Fig. 7) may contain such systems, even though the driving mech-  
924 anisms are different from those of MCSs.

925 The mechanisms for organisation of convection over and close to the TP are most  
926 likely very different from MCS formation over the plains, because of the influence of moun-  
927 tain barriers, local wind systems and the orographically modified large-scale circulation.  
928 The distinct diurnal evolution of MCSs that are initiated over the TP (Fig. 9) and the  
929 large contributions of small-scale convective cells (TCSs) to precipitation (Fig. 11) em-  
930 phasise the importance of local conditions and topography. The dominating pattern for  
931 MCS initiation over the TP in the afternoon hours compared to the diversified patterns  
932 in the surroundings (Fig. 9) is consistent with Zheng et al. (2008), who found that single-  
933 peak MCSs are more common over mountains and plateaus whereas multi-peak MCSs  
934 are more common over basins and plains. This means that convection over the TP is closely  
935 related to the diurnal flow patterns and surface heating, whereas MCSs in the TPB re-  
936 gion and over the ocean do not occur at a specific time of the day. In the same study,  
937 the authors concluded that multi-peak MCSs also correspond to longer-lived MCSs and  
938 MCSs with larger horizontal dimensions. This is also consistent with our findings, as the  
939 second peak in the initiation times for all MCSs (Fig. 8b) can be mainly attributed to  
940 LE systems that are more long-lived, larger and generally more intense than MCS over  
941 the TP (Fig. 14).

942 An important trigger mechanism for organised convection over and close to the moun-  
943 tains could be frequently occurring are mesoscale disturbances in vorticity around 500  
944 hPa, namely Tibetan Plateau vortices (TPVs) (Feng et al., 2017; Hunt et al., 2018; Cu-  
945 rio et al., 2019). While the presence and strength of TPVs is not clearly distinguishable  
946 in the mean geopotential field at 5,000 hPa for MCS composites over the TP (Fig. 16a-  
947 b), this study shows that MCSs that are initiated over the TP are clearly associated with  
948 positive anomalies of the upper-level westerly jet. This large-scale feature is most likely  
949 also linked to the occurrence frequency and intensity of TPVs, as Curio et al. (2019) showed  
950 that the position and strength of the westerly jet controls the travel distance of TPVs.  
951 The TP is usually marked by limited moisture supply and CAPE (Fig. 18a-b), which  
952 show strong positive anomalies when MCSs are initiated over the high altitudes. This  
953 means that the intensified westerly jet may create favourable conditions for enhanced  
954 moisture supply and dynamic/thermodynamic disturbances, such as TPVs. Furthermore,  
955 it has been suggested in many studies that TPVs are important precipitation-bearing  
956 systems for the TP. For instance, Curio et al. (2019) demonstrated that a significant part  
957 of the plateau-scale precipitation occurs within a  $3^\circ$  radius of tracked TPV centres. The  
958 results from this study suggest, however, that the precipitation and cloud features identi-  
959 fiable in satellite observations occur at smaller scales and less frequently over high al-

960 titudes than TPVs. This suggests that the relationship between mesoscale disturbances  
961 in vorticity and organisation of convection is more complex than assuming that TPVs  
962 always result in well-developed MCSs. Future studies on the linkages between TPVs and  
963 observed MCS features as well as isolated deep convection, could provide valuable in-  
964 sights into mesoscale dynamics over the TP, as TPVs may also affect the water vapor  
965 transport to and from the TP.

966 The systems that made the greatest contributions to precipitation  $>5 \text{ mm h}^{-1}$  over  
967 the TP (including both MCSs and TCSs) were located in the eastern part of the TP. This  
968 regional pattern may be related to surface properties, such as soil moisture and vegeta-  
969 tion, which can regulate heat fluxes in the boundary layer (Talib et al., 2021) and thereby  
970 increase the convective instability at higher altitudes. This has, for instance, been sug-  
971 gested by Sugimoto and Ueno (2012) who found that soil moisture played a crucial role  
972 for convection initiation over the eastern TP. Barton et al. (2021) found that regions with  
973 higher soil moisture favour strong convection over the TP, but that vegetation, topog-  
974 raphy and background winds are additional factors that affect this relationship. Out-  
975 side of the monsoon season, only very few systems have been detected. The few cloud  
976 clusters with a heavy rain core during the cold season are therefore probably driven by  
977 other mechanisms than organisation of convection, such as the lake-effect, which has been  
978 shown to trigger severe snow storms over the TP (Dai et al., 2020).

979 The complex patterns of MCSs at different spatial scales and highly varying pre-  
980 cipitation features summarised in this study suggest that convection-permitting simu-  
981 lations are needed to provide a more complete picture of the underlying dynamics for  
982 precipitation formation in the TP region. In other regions, such as North America, it  
983 has been shown that convection-permitting simulations realistically capture the main char-  
984 acteristics of MCSs and associated precipitation (Prein et al., 2017). Such simulations  
985 could hence be a promising tool to understand the essential ingredients for mountain con-  
986 vection to organize into larger systems. So far, there are no studies that have looked at  
987 MCSs over the TP and in the TP downstream regions using model simulations with spa-  
988 tial resolutions finer than 30 km, although a few simulations with finer resolutions ex-  
989 ist (Ou et al., 2020; Zhou et al., 2021). The existing and future fine resolution mod-  
990 elling over the TP should be used to explore the dynamics of the MCSs, in order to effectively  
991 represent small convective features in the TP downstream region, particularly those which  
992 are close to the 3,000 m boundary and interact with the topography.

## 993 5 Summary and conclusions

994 This study provides an observational perspective of MCSs in the TP region and  
995 elucidates the role of MCSs in seasonal and heavy precipitation. We tracked MCSs by  
996 co-locating brightness temperatures from IR satellite imagery and precipitation estimates  
997 from GPM IMERG for the period 2000 – 2019. Spatial and temporal characteristics of  
998 MCS tracks, their associated precipitation features and large-scale atmospheric environ-  
999 ments were examined over the TP, around the TPB and in the LE region.

1000 By comparing four different tracking methods, we have shown that it is useful to  
1001 apply additional criteria that assure the development of deep convection and heavy pre-  
1002 cipitation, when IR brightness temperature thresholds are used to track MCSs in satel-  
1003 lite imagery. To be considered a MCS in this study, cloud features (defined as a region  
1004  $\leq 221 \text{ K}$  over  $50,000 \text{ km}^2$ ) had to persist for at least 3 hours. In addition, the connected  
1005 cloud features had to contain a region with brightness temperatures below 200 K and  
1006 a region with rain rates  $\geq 5 \text{ mm h}^{-1}$  that extends over at least 10 % of the minimum  
1007 cloud area. These extra criteria significantly reduced the number of falsely identified MCSs  
1008 as a consequence of the presence of cirrus clouds or cold surfaces in high mountain re-  
1009 gions and results in a more realistic seasonal cycle for MCS frequency with a distinct sum-  
1010 mer peak. Most of the cases which showed a drop in brightness temperature  $< 200 \text{ K}$

1011 also contained a core with heavy rain and consequently the number of classified MCS  
1012 tracks reduced only slightly for  $T_b$  heavy rain core compared to  $T_b$  cold core. These two  
1013 criteria also resulted in the same key statistics, which means that they can be used in-  
1014 terchangeably, but the use of both precipitation and brightness temperature data remains  
1015 advantageous because it allows precipitation features to be identified and examined in  
1016 the tracked clouds cells.

1017 Most of the MCSs identified using our tracking method were found over the Indian  
1018 subcontinent and Bay of Bengal. Over the oceans, MCS contributed to more than 80  
1019 % of the total precipitation during the onset of the Indian summer monsoon (May-June).  
1020 Regions over land, where MCSs account for more than 50 % of the total precipitation  
1021 between July and August were the Indo-Gangetic Plain, the southern foothills of the Hi-  
1022 malayan mountain range as well as the Sichuan and Yangtze river basins. Our results  
1023 showed also that MCSs with the highest amounts of total heavy precipitation were char-  
1024 acterised by longevity and large cloud extents rather than by high intensities.

1025 MCSs over the TP and at the TPB were generally less frequent compared to the  
1026 LE region. We detected substantial differences in the diurnal evolution, longevity, pre-  
1027 cipitation features and large-scale atmospheric environments between MCSs that inter-  
1028 act with the mountains (TPB + TP) and MCSs in the LE region. One notable charac-  
1029 teristic of the large-scale environments that was associated with MCS initiation over the  
1030 TP was, for instance, the intensification of the anticyclonic circulation around the South  
1031 Asin High accompanied with positive water vapor transport along the Himalayas and  
1032 increased CAPE over the TP and China. Furthermore, we have shown that the contri-  
1033 bution of MCS-induced precipitation to the total summer precipitation (total heavy pre-  
1034 cipitation) over most parts of the TP corresponded to 10 - 20% (20 - 50%) in July, but  
1035 below 10 % (30 %) during the other monsoon months. Even though the MCS contribu-  
1036 tion to total heavy summer precipitation over the TP was significantly higher than the  
1037 MCS contribution to total summer precipitation, it was still significantly lower than in  
1038 most of the LE region. This is consistent with our result that MCSs over the TP were  
1039 generally less frequent, smaller and more short-lived, and can most likely be attributed  
1040 to the limited moisture supply over the mountains. Convective systems at the meso- $\beta$ -  
1041 scale showed higher contributions to the total and heavy precipitation over the TP dur-  
1042 ing summer than the larger MCSs. This finding highlights the significance of more lo-  
1043 calised precipitation systems and convective modes for the water cycle over the TP, in  
1044 contrast to large convective clusters which occur mainly in the downstream regions south  
1045 and east of the TP. Model simulations at convective scales may have the potential to im-  
1046 prove the understanding of mesoscale dynamics for precipitation formation over the TP.

### 1047 Acknowledgments

1048 We thank three anonymous reviewers for their constructive comments and suggestions.  
1049 The study was supported by the Swedish National Space Agency (SNSA: 188/18 4) and  
1050 the Chinese Academy of Sciences (XDA2006040103). It is a contribution no 7 to CORDEX-  
1051 FPS-CPTP and Swedish MERGE. We thank the providers of key datasets used here (NASA,  
1052 NCEP). NCEP/CPC Brightness temperatures can be downloaded from [https://disc](https://disc.gsfc.nasa.gov/datasets/GPM_MERGIR_V1/summary)  
1053 [.gsfc.nasa.gov/datasets/GPM\\_MERGIR\\_V1/summary](https://disc.gsfc.nasa.gov/datasets/GPM_MERGIR_V1/summary) and GPM IMERG v06 can be down-  
1054 loaded from [https://disc.gsfc.nasa.gov/datasets/GPM\\_3IMERGHH\\_06/summary](https://disc.gsfc.nasa.gov/datasets/GPM_3IMERGHH_06/summary) or  
1055 from <https://gpm.nasa.gov/data/directory>. The latest version of the hourly ERA5  
1056 reanalysis at pressure levels can be accessed through Copernicus Climate Data Store:  
1057 [https://cds.climate.copernicus.eu/cdsapp#!/dataset/reanalysis-era5-pressure](https://cds.climate.copernicus.eu/cdsapp#!/dataset/reanalysis-era5-pressure-levels?tab=overview)  
1058 [-levels?tab=overview](https://cds.climate.copernicus.eu/cdsapp#!/dataset/reanalysis-era5-pressure-levels?tab=overview).

1059 The MCS dataset can be downloaded in form of annual files at [https://doi.org/](https://doi.org/10.5281/zenodo.4767152)  
1060 [10.5281/zenodo.4767152](https://doi.org/10.5281/zenodo.4767152).

1061 The code for the MCS tracking algorithm can be found at [https://github.com/](https://github.com/JuliaKukulies/mcs_tracking/tree/master/CTT/tracking)  
 1062 [JuliaKukulies/mcs\\_tracking/tree/master/CTT/tracking](https://github.com/JuliaKukulies/mcs_tracking/tree/master/CTT/tracking).

## 1063 References

- 1064 Ban, N., Schmidli, J., & Schär, C. (2015). Heavy precipitation in a changing cli-  
 1065 mate: Does short-term summer precipitation increase faster? *Geophysical Re-*  
 1066 *search Letters*, *42*(4), 1165–1172.
- 1067 Barton, E., Taylor, C., Klein, C., Harris, P., & Meng, X. (2021). Observed soil mois-  
 1068 ture impact on strong convection over mountainous tibetan plateau. *Journal of*  
 1069 *Hydrometeorology*, *22*(3), 561–572.
- 1070 Berg, P., Moseley, C., & Haerter, J. O. (2013). Strong increase in convective precipi-  
 1071 tation in response to higher temperatures. *Nature Geoscience*, *6*(3), 181–185.
- 1072 Bibi, S., Wang, L., Li, X., Zhou, J., Chen, D., & Yao, T. (2018). Climatic and asso-  
 1073 ciated cryospheric, biospheric, and hydrological changes on the tibetan plateau:  
 1074 a review. *International Journal of Climatology*, *38*, e1–e17.
- 1075 Boos, W. R., Mapes, B. E., & Murthy, V. S. (2017). Potential vorticity structure  
 1076 and propagation mechanism of indian monsoon depressions. In *The global*  
 1077 *monsoon system: Research and forecast* (pp. 187–199). World Scientific.
- 1078 Cheeks, S. M., Fueglistaler, S., & Garner, S. T. (2020). A satellite-based climatology  
 1079 of central and southeastern us mesoscale convective systems. *Monthly Weather*  
 1080 *Review*, *148*(6), 2607–2621.
- 1081 Chen, D., Guo, J., Yao, D., Lin, Y., Zhao, C., Min, M., . . . Chen, T. (2019).  
 1082 Mesoscale convective systems in the asian monsoon region from advanced  
 1083 himawari imager: Algorithms and preliminary results. *Journal of Geophysical*  
 1084 *Research: Atmospheres*, *124*(4), 2210–2234.
- 1085 Cheng, C.-P., & Houze, R. A. (1979). The distribution of convective and mesoscale  
 1086 precipitation in gate radar echo patterns. *Monthly Weather Review*, *107*(10),  
 1087 1370–1381.
- 1088 Cui, W., Dong, X., Xi, B., Feng, Z., & Fan, J. (2020). Can the gpm imerg final  
 1089 product accurately represent mcs precipitation characteristics over the central  
 1090 and eastern united states? *Journal of Hydrometeorology*, *21*(1), 39–57.
- 1091 Cui, W., Dong, X., Xi, B., & Liu, M. (2020). Cloud and precipitation properties  
 1092 of mcs along the meiyu frontal zone in central and southern china and their  
 1093 associated large-scale environments. *Journal of Geophysical Research: Atmo-*  
 1094 *spheres*, *125*(6), e2019JD031601.
- 1095 Curio, J., Chen, Y., Schiemann, R., Turner, A. G., Wong, K. C., Hodges, K., & Li,  
 1096 Y. (2018). Comparison of a manual and an automated tracking method for  
 1097 tibetan plateau vortices. *Advances in Atmospheric Sciences*, *35*(8), 965–980.
- 1098 Curio, J., Schiemann, R., Hodges, K. I., & Turner, A. G. (2019). Climatology of  
 1099 tibetan plateau vortices in reanalysis data and a high-resolution global climate  
 1100 model. *Journal of Climate*, *32*(6), 1933–1950.
- 1101 Dai, Y., Chen, D., Yao, T., & Wang, L. (2020). Large lakes over the tibetan plateau  
 1102 may boost snow downwind: implications for snow disaster. *Science Bulletin*.
- 1103 Diaz, M., & Boos, W. R. (2019). Barotropic growth of monsoon depressions. *Quar-*  
 1104 *terly Journal of the Royal Meteorological Society*, *145*(719), 824–844.
- 1105 Duan, Y., Wilson, A. M., & Barros, A. P. (2015). Scoping a field experiment: Error  
 1106 diagnostics of trmm precipitation radar estimates in complex terrain as a basis  
 1107 for iphex2014. *Hydrology and Earth System Sciences*, *19*(3), 1501–1520.
- 1108 Esmaili, R. B., Tian, Y., Vila, D. A., & Kim, K.-M. (2016). A lagrangian analysis of  
 1109 cold cloud clusters and their life cycles with satellite observations. *Journal of*  
 1110 *Geophysical Research: Atmospheres*, *121*(19), 11–723.
- 1111 Feidas, H. (2017). Satellite-observed features of a mesoscale convective complex over  
 1112 se europe. *International Journal of Remote Sensing*, *38*(22), 6219–6246.

- 1113 Feng, X., Liu, C., Fan, G., & Zhang, J. (2017). Analysis of the structure of different  
1114 tibetan plateau vortex types. *Journal of Meteorological Research*, 31(3), 514–  
1115 529.
- 1116 Feng, Z., Leung, L. R., Houze Jr, R. A., Hagos, S., Hardin, J., Yang, Q., ... Fan, J.  
1117 (2018). Structure and evolution of mesoscale convective systems: Sensitivity to  
1118 cloud microphysics in convection-permitting simulations over the united states.  
1119 *Journal of Advances in Modeling Earth Systems*, 10(7), 1470–1494.
- 1120 Feng, Z., Leung, R., Liu, N., Wang, J., Houze, R., Li, J., ... Guo, J. (2021). A  
1121 global high-resolution mesoscale convective system database using satellite-  
1122 derived cloud tops, surface precipitation, and tracking. *Journal of Geophysical*  
1123 *Research: Atmospheres*, e2020JD034202.
- 1124 Fitzpatrick, R. G., Parker, D. J., Marsham, J. H., Rowell, D. P., Guichard, F. M.,  
1125 Taylor, C. M., ... others (2020). What drives the intensification of mesoscale  
1126 convective systems over the west african sahel under climate change? *Journal*  
1127 *of Climate*, 33(8), 3151–3172.
- 1128 Flohn, H., & Reiter, E. R. (1968). Contributions to a meteorology of the tibetan  
1129 highlands. *Atmospheric science paper; no. 130*.
- 1130 Fritsch, J., Kane, R., & Chelius, C. (1986). The contribution of mesoscale convective  
1131 weather systems to the warm-season precipitation in the united states. *Journal*  
1132 *of climate and applied meteorology*, 25(10), 1333–1345.
- 1133 Gaál, L., Molnar, P., & Szolgay, J. (2014). Selection of intense rainfall events based  
1134 on intensity thresholds and lightning data in switzerland. *Hydrology and Earth*  
1135 *System Sciences*, 18(5), 1561–1573.
- 1136 Guo, Z.-y., Dai, X.-y., Wu, J.-p., & Lin, H. (2006). Analysis of mesoscale convective  
1137 systems over tibetan plateau in summer. *Chinese Geographical Science*, 16(2),  
1138 116–121.
- 1139 Heikenfeld, M., Marinescu, P. J., Christensen, M., Watson-Parris, D., Senf, F., Van  
1140 Den Heever, S. C., & Stier, P. (2019). tobac v1. 0: towards a flexible frame-  
1141 work for tracking and analysis of clouds in diverse datasets. *Geoscientific*  
1142 *Model Development Discussions*.
- 1143 Hersbach, H., Bell, B., Berrisford, P., Hirahara, S., Horányi, A., Muñoz-Sabater, J.,  
1144 ... others (2020). The era5 global reanalysis. *Quarterly Journal of the Royal*  
1145 *Meteorological Society*, 146(730), 1999–2049.
- 1146 Hitchcock, S. M., Schumacher, R. S., Herman, G. R., Coniglio, M. C., Parker, M. D.,  
1147 & Ziegler, C. L. (2019). Evolution of pre-and postconvective environmental  
1148 profiles from mesoscale convective systems during pecan. *Monthly Weather*  
1149 *Review*, 147(7), 2329–2354.
- 1150 Houze, R. A., Wilton, D. C., & Smull, B. F. (2007). Monsoon convection in the  
1151 himalayan region as seen by the trmm precipitation radar. *Quarterly Journal*  
1152 *of the Royal Meteorological Society: A journal of the atmospheric sciences,*  
1153 *applied meteorology and physical oceanography*, 133(627), 1389–1411.
- 1154 Houze Jr, R. A. (2004). Mesoscale convective systems. *Reviews of Geophysics*,  
1155 42(4).
- 1156 Hu, H., Leung, R., & Feng, Z. (2020). Observed warm-season characteristics of mcs  
1157 and non-mcs rainfall and their recent changes in the central united states. *Geo-*  
1158 *physical Research Letters*, 47(6), e2019GL086783.
- 1159 Huang, X., Hu, C., Huang, X., Chu, Y., Tseng, Y.-h., Zhang, G. J., & Lin, Y.  
1160 (2018). A long-term tropical mesoscale convective systems dataset based  
1161 on a novel objective automatic tracking algorithm. *Climate dynamics*, 51(7),  
1162 3145–3159.
- 1163 Huffman, G., Stocker, E., Bolvin, D., Nelkin, E., & Jackson, T. (2019). Gpm imerg  
1164 final precipitation l3 half hourly 0.1 degree x 0.1 degree v06. *Greenbelt, MD,*  
1165 *Goddard Earth Sciences Data and Information Services Center (GES DISC)*.
- 1166 Hunt, K., Curio, J., Turner, A., & Schiemann, R. (2018). Subtropical westerly jet  
1167 influence on occurrence of western disturbances and tibetan plateau vortices.

- 1168 *Geophysical Research Letters*, 45(16), 8629–8636.
- 1169 Hurley, J. V., & Boos, W. R. (2015). A global climatology of monsoon low-pressure  
1170 systems. *Quarterly Journal of the Royal Meteorological Society*, 141(689),  
1171 1049–1064.
- 1172 Janowiak, J., Joyce, B., & Xie, P. (2017). Ncep/cpc l3 half hourly 4km global (60s  
1173 - 60n) merged ir v1. *Edited by Andrey Savtchenko, Greenbelt, MD, Goddard*  
1174 *Earth Sciences Data and Information Services Center (GES DISC)*.
- 1175 Jia, X., & Yang, S. (2013). Impact of the quasi-biweekly oscillation over the western  
1176 north pacific on east asian subtropical monsoon during early summer. *Journal*  
1177 *of Geophysical Research: Atmospheres*, 118(10), 4421–4434.
- 1178 Jiang, J.-x., & Fan, M.-z. (2002). Convective clouds and mesoscale convective  
1179 systems over the tibetan plateau in summer. *Chin. J. Atmos. Sci.*, 26(2),  
1180 263–270.
- 1181 Kirkpatrick, C., McCaul Jr, E. W., & Cohen, C. (2011). Sensitivities of simulated  
1182 convective storms to environmental cape. *Monthly weather review*, 139(11),  
1183 3514–3532.
- 1184 Klein, C., Belušić, D., & Taylor, C. M. (2018). Wavelet scale analysis of mesoscale  
1185 convective systems for detecting deep convection from infrared imagery. *Jour-*  
1186 *nal of Geophysical Research: Atmospheres*, 123(6), 3035–3050.
- 1187 Kukulies, J., Chen, D., & Wang, M. (2019). Temporal and spatial variations of  
1188 convection and precipitation over the tibetan plateau based on recent satel-  
1189 lite observations. part i: Cloud climatology derived from cloudsat and calipso.  
1190 *International Journal of Climatology*, 39(14), 5396–5412.
- 1191 Kukulies, J., Chen, D., & Wang, M. (2020). Temporal and spatial variations of con-  
1192 vection, clouds and precipitation over the tibetan plateau from recent satellite  
1193 observations. part ii: Precipitation climatology derived from global precipita-  
1194 tion measurement mission. *International Journal of Climatology*.
- 1195 Lai, H.-W., Chen, H. W., Kukulies, J., Ou, T., & Chen, D. (2021). Regionalization  
1196 of seasonal precipitation over the tibetan plateau and associated large-scale  
1197 atmospheric systems. *Journal of Climate*, 34(7), 2635–2651.
- 1198 Li, L., Zhang, R., Wen, M., & Liu, L. (2014). Effect of the atmospheric heat source  
1199 on the development and eastward movement of the tibetan plateau vortices.  
1200 *Tellus A: Dynamic Meteorology and Oceanography*, 66(1), 24451.
- 1201 Li, P., Moseley, C., Prein, A. F., Chen, H., Li, J., Furtado, K., & Zhou, T. (2020).  
1202 Mesoscale convective system precipitation characteristics over east asia. part  
1203 i: regional differences and seasonal variations. *Journal of Climate*, 33(21),  
1204 9271–9286.
- 1205 Li, Y., Yun, W., Yang, S., Liang, H., Shouting, G., & Fu. (2008). Characteristics of  
1206 summer convective systems initiated over the tibetan plateau. part i: Origin,  
1207 track, development, and precipitation. *Journal of applied meteorology and*  
1208 *climatology*, 47(10), 2679–2695.
- 1209 Ma, Y., Tang, G., Long, D., Yong, B., Zhong, L., Wan, W., & Hong, Y. (2016).  
1210 Similarity and error intercomparison of the gpm and its predecessor-trmm mul-  
1211 tisatellite precipitation analysis using the best available hourly gauge network  
1212 over the tibetan plateau. *Remote sensing*, 8(7), 569.
- 1213 Maddox, R. A. (1980). Mesoscale convective complexes. *Bulletin of the American*  
1214 *Meteorological Society*, 1374–1387.
- 1215 Mai, Z., Fu, S.-M., Sun, J.-H., Hu, L., & Wang, X.-m. (2021). Key statistical charac-  
1216 teristics of the mesoscale convective systems generated over the tibetan plateau  
1217 and their relationship to precipitation and southwest vortices. *International*  
1218 *Journal of Climatology*, 41, E875–E896.
- 1219 Morel, C., & Senesi, S. (2002). A climatology of mesoscale convective systems  
1220 over europe using satellite infrared imagery. ii: Characteristics of european  
1221 mesoscale convective systems. *Quarterly Journal of the Royal Meteorologi-*  
1222 *cal Society: A journal of the atmospheric sciences, applied meteorology and*

- 1223 *physical oceanography*, 128(584), 1973–1995.
- 1224 Orlanski, I. (1975). A rational subdivision of scales for atmospheric processes. *Bul-*  
 1225 *letin of the American Meteorological Society*, 527–530.
- 1226 Ou, T., Chen, D., Chen, X., Lin, C., Yang, K., Lai, H.-W., & Zhang, F. (2020).  
 1227 Simulation of summer precipitation diurnal cycles over the tibetan plateau at  
 1228 the gray-zone grid spacing for cumulus parameterization. *Climate Dynamics*,  
 1229 54(7), 3525–3539.
- 1230 Prein, A., Liu, C., Ikeda, K., Bullock, R., Rasmussen, R. M., Holland, G. J., &  
 1231 Clark, M. (2017). Simulating north american mesoscale convective systems  
 1232 with a convection-permitting climate model. *Climate Dynamics*, 1–16.
- 1233 Rasmussen, K., & Houze, R. (2012). A flash-flooding storm at the steep edge of high  
 1234 terrain: disaster in the himalayas. *Bulletin of the American Meteorological So-*  
 1235 *ciety*, 93(11), 1713–1724.
- 1236 Redelsperger, J.-L., Diongue, A., Diedhiou, A., Ceron, J.-P., Diop, M., Gueremy,  
 1237 J.-F., & Lafore, J.-P. (2002). Multi-scale description of a sahelian synoptic  
 1238 weather system representative of the west african monsoon. *Quarterly Journal*  
 1239 *of the Royal Meteorological Society: A journal of the atmospheric sciences,*  
 1240 *applied meteorology and physical oceanography*, 128(582), 1229–1257.
- 1241 Ren, X., Yang, D., & Yang, X.-Q. (2015). Characteristics and mechanisms of the  
 1242 subseasonal eastward extension of the south asian high. *Journal of Climate*,  
 1243 28(17), 6799–6822.
- 1244 Roebber, P. J., Schultz, D. M., & Romero, R. (2002). Synoptic regulation of the 3  
 1245 may 1999 tornado outbreak. *Weather and Forecasting*, 17(3), 399–429.
- 1246 Romatschke, U., Medina, S., & Houze, R. (2010). Regional, seasonal, and diurnal  
 1247 variations of extreme convection in the south asian region. *Journal of climate*,  
 1248 23(2), 419–439.
- 1249 Rossow, W. B., & Schiffer, R. A. (1999). Advances in understanding clouds from is-  
 1250 ccp. *Bulletin of the American Meteorological Society*, 80(11), 2261–2288.
- 1251 Rutledge, S. A., & Houze Jr, R. A. (1987). A diagnostic modelling study of the trail-  
 1252 ing stratiform region of a midlatitude squall line. *Journal of the atmospheric*  
 1253 *sciences*, 44(18), 2640–2656.
- 1254 Schädlich, S., Göttsche, F., & Olesen, F.-S. (2001). Influence of land surface pa-  
 1255 rameters and atmosphere on meteosat brightness temperatures and generation  
 1256 of land surface temperature maps by temporally and spatially interpolating  
 1257 atmospheric correction. *Remote Sensing of Environment*, 75(1), 39–46.
- 1258 Schiemann, R., Lüthi, D., & Schär, C. (2009). Seasonality and interannual vari-  
 1259 ability of the westerly jet in the tibetan plateau region. *Journal of climate*,  
 1260 22(11), 2940–2957.
- 1261 Shang, W., Ren, X., Huang, B., Cubasch, U., & Yang, X.-Q. (2019). Subseasonal  
 1262 intensity variation of the south asian high in relationship to diabatic heating:  
 1263 observation and cmip5 models. *Climate Dynamics*, 52(3), 2413–2430.
- 1264 Shi, X., Wang, Y., & Xu, X. (2008). Effect of mesoscale topography over the tibetan  
 1265 plateau on summer precipitation in china: A regional model study. *Geophysical*  
 1266 *Research Letters*, 35(19).
- 1267 Song, F., Feng, Z., Leung, L. R., Houze Jr, R. A., Wang, J., Hardin, J., & Homeyer,  
 1268 C. R. (2019). Contrasting spring and summer large-scale environments asso-  
 1269 ciated with mesoscale convective systems over the us great plains. *Journal of*  
 1270 *Climate*, 32(20), 6749–6767.
- 1271 Sugimoto, S., & Ueno, K. (2012). Role of mesoscale convective systems developed  
 1272 around the eastern tibetan plateau in the eastward expansion of an upper  
 1273 tropospheric high during the monsoon season. *Journal of the Meteorological*  
 1274 *Society of Japan. Ser. II*, 90(2), 297–310.
- 1275 Talib, J., Taylor, C. M., Duan, A., & Turner, A. G. (2021). Intraseasonal soil  
 1276 moisture–atmosphere feedbacks on the tibetan plateau circulation. *Journal of*  
 1277 *Climate*, 34(5), 1789–1807.

- 1278 Tao, S.-y., & Ding, Y.-h. (1981). Observational evidence of the influence of the  
1279 qinghai-xizang (tibet) plateau on the occurrence of heavy rain and severe  
1280 convective storms in china. *Bulletin of the American Meteorological Society*,  
1281 *62*(1), 23–30.
- 1282 Vondou, D. A., Nzeukou, A., & Kamga, F. M. (2010). Diurnal cycle of convective  
1283 activity over the west of central africa based on meteosat images. *International*  
1284 *journal of applied earth observation and geoinformation*, *12*, S58–S62.
- 1285 Wang, B. (1987). The development mechanism for tibetan plateau warm vortices.  
1286 *Journal of the atmospheric sciences*, *44*(20), 2978–2994.
- 1287 Wang, C., Luo, J., Rossow, W. B., & Pearl, C. (2018). Production of globally uni-  
1288 form isccp convection tracking (ct) dataset and preliminary analysis results.  
1289 *AGUFM*, *2018*, A11J–2361.
- 1290 Wen, Y., Behrangi, A., Lambrigtsen, B., & Kirstetter, P.-E. (2016). Evaluation  
1291 and uncertainty estimation of the latest radar and satellite snowfall products  
1292 using snotel measurements over mountainous regions in western united states.  
1293 *Remote Sensing*, *8*(11), 904.
- 1294 Xiang, S., Li, Y., Li, D., & Yang, S. (2013). An analysis of heavy precipitation  
1295 caused by a retracing plateau vortex based on trmm data. *Meteorology and At-*  
1296 *mospheric Physics*, *122*(1-2), 33–45.
- 1297 Xu, R., Tian, F., Yang, L., Hu, H., Lu, H., & Hou, A. (2017). Ground validation of  
1298 gpm imerg and trmm 3b42v7 rainfall products over southern tibetan plateau  
1299 based on a high-density rain gauge network. *Journal of Geophysical Research:*  
1300 *Atmospheres*, *122*(2), 910–924.
- 1301 Xu, W., & Zipser, E. J. (2011). Diurnal variations of precipitation, deep convection,  
1302 and lightning over and east of the eastern tibetan plateau. *Journal of Climate*,  
1303 *24*(2), 448–465.
- 1304 Yang, R., Zhang, Y., Sun, J., Fu, S., & Li, J. (2019). The characteristics and clas-  
1305 sification of eastward-propagating mesoscale convective systems generated  
1306 over the second-step terrain in the yangtze river valley. *Atmospheric Science*  
1307 *Letters*, *20*(1), e874.
- 1308 Yao, T., Xue, Y., Chen, D., Chen, F., Thompson, L., Cui, P., ... others (2019). Re-  
1309 cent third poles rapid warming accompanies cryospheric melt and water cycle  
1310 intensification and interactions between monsoon and environment: Multidis-  
1311 ciplinary approach with observations, modeling, and analysis. *Bulletin of the*  
1312 *American Meteorological Society*, *100*(3), 423–444.
- 1313 Yasunari, T., & Miwa, T. (2006). Convective cloud systems over the tibetan plateau  
1314 and their impact on meso-scale disturbances in the meiyu/baiu frontal zone.  
1315 *Journal of the Meteorological Society of Japan. Ser. II*, *84*(4), 783–803.
- 1316 Ye, D.-Z., & Wu, G.-X. (1998). The role of the heat source of the tibetan plateau  
1317 in the general circulation. *Meteorology and Atmospheric Physics*, *67*(1-4), 181–  
1318 198.
- 1319 Yuan, J., & Houze, R. (2010). Global variability of mesoscale convective system  
1320 anvil structure from a-train satellite data. *Journal of Climate*, *23*(21), 5864–  
1321 5888.
- 1322 Zhang, L., Su, F., Yang, D., Hao, Z., & Tong, K. (2013). Discharge regime and sim-  
1323 ulation for the upstream of major rivers over tibetan plateau. *Journal of Geo-*  
1324 *physical Research: Atmospheres*, *118*(15), 8500–8518.
- 1325 Zhang, S., Wang, D., Qin, Z., Zheng, Y., & Guo, J. (2018). Assessment of the gpm  
1326 and trmm precipitation products using the rain gauge network over the tibetan  
1327 plateau. *Journal of Meteorological Research*, *32*(2), 324–336.
- 1328 Zheng, Y., Chen, J., & Zhu, P. (2008). Climatological distribution and diurnal  
1329 variation of mesoscale convective systems over china and its vicinity during  
1330 summer. *Chinese Science Bulletin*, *53*(10), 1574–1586.
- 1331 Zhou, X., Yang, K., Ouyang, L., Wang, Y., Jiang, Y., Li, X., ... Prein, A. (2021).  
1332 Added value of kilometer-scale modeling over the third pole region: a cordex-

Accepted Article